Investigation of Aspects of Aeroservoelastic State-Space Modeling on Active Flutter Suppression LQR Control Synthesis

Andrew D. Phillips

A thesis submitted in partial fulfillment of the requirements for the degree of

Master of Science in Aeronautics & Astronautics

University of Washington

2018

Reading Committee:

Eli Livne, Chair

Kristi A. Morgansen

Program Authorized to Offer Degree:
William E. Boeing Department of Aeronautics and Astronautics

University of Washington

Abstract

Investigation of Aspects of Aeroservoelastic State-Space Modeling on Active Flutter Suppression LQR Control Synthesis

Andrew D. Phillips

Chair of the Supervisory Committee:
Professor Eli Livne
William E. Boeing Department of Aeronautics and Astronautics

Whether motivated by cost or performance, the shift to structurally lighter aircraft has increased the demand for new developments in aeroservoelasticity. The William E. Boeing Department of Aeronautics and Astronautics has invested significant resources to meet this demand, involving wind tunnel models and modifications, and software development. A major step in aeroservoelastic analysis is the generation of the required state-space models. This thesis describes the development of a MATLAB code with such a capability. The code is intended to be modified and used by the department for future research. This in-house capability allows for greater flexibility and transparency for future users. Two numerical experiments were run using the new code. The focus was the effect of actuator model's order and the range of reduced frequencies used to generate rational function approximation in the form of a Roger series. It was determined that the order of actuation models and the range of reduced frequencies used in a Roger Approximation had little to no effect on Linear-Quadratic Regulator synthesis and performance for Active Flutter Suppression of a wing/flap system investigated in this work.

TABLE OF CONTENTS

Page

List of Figures iii

List of Tables v

Chapter 1: Introduction 1
1.1 Motivation 1
1.2 Objective 2
1.3 Need 2

Chapter 2: Theory 3
2.1 Equations of Motion 3
2.2 Structures 5
2.3 Aerodynamics 6
2.4 Splining 7
2.5 Rational Function Approximation 8
2.6 State-Space Representation 11

Chapter 3: MATLAB Code Description 19

Chapter 4: Test System Description 21
4.1 Duke University wing/flap system 21
4.2 Actuators 24

Chapter 5: Results 27
5.1 Case 1 : Perfect Actuator - 80% *Flutter* 30
5.2 Case 2 : Perfect Actuator - 120% *Flutter* 33
5.3 Case 3 : LOA - 80% *Flutter* 36
5.4 Case 4 : LOA - 120% *Flutter* 39

5.5 Case 5 : HOA - 80% *Flutter* 42
5.6 Case 6 : HOA - 120% *Flutter* 45
5.7 Case 7 : HOA - 120% *Flutter* - $2 \times k_{max}$ 48

Chapter 6: Discussion 51
6.1 Controllability and Observability 51
6.2 Lessons Learned 52

Chapter 7: Conclusion 54
7.1 Recommendations 54

Bibliography 55

Appendix A: Poles and Zeros 56

Appendix B: Controllability and Observability 60

LIST OF FIGURES

Figure Number		Page
1.1	B-52 AFS vehicle.	2
2.1	Sketch of transport aircraft FEM grid and mode shape.	6
2.2	Typical Panel Model of a wing-body configuration.	7
2.3	Spline axis along the axis of wing-like component.	8
3.1	MATLAB code flowchart.	20
4.1	Duke University wing/flap system design.	21
4.2	Sensor placement on wing/flap system.	23
4.3	F/A-18 HARV TVCS aircraft in flight.	24
4.4	Actuator comparison Bode plots - Output q_c.	25
4.5	Actuator comparison Bode plots - Output sq_c.	26
4.6	Actuator comparison Bode plots - Output s^2q_c.	26
5.1	Roger approximation comparison to actual data. Perfect, k_{set1}	28
5.2	Roger approximation comparison to actual data. Perfect, k_{set2}	29
5.3	System poles and zeros. Perfect, 80% flutter speed.	30
5.4	Time response to 2 degree perturbation in α. Perfect, 80% flutter speed.	31
5.5	Frequency response. Perfect, 80% flutter speed.	32
5.6	System poles and zeros. Perfect, 120% flutter speed.	33
5.7	Time response to 2 degree perturbation in α. Perfect, 120% flutter speed.	34
5.8	Frequency response. Perfect, 120% flutter speed.	35
5.9	System poles and zeros. LOA, 80% flutter speed.	36
5.10	Time response to 2 degree perturbation in α. LOA, 80% flutter speed.	37
5.11	Frequency response. LOA, 80% flutter speed.	38
5.12	System poles and zeros. LOA, 120% flutter speed.	39
5.13	Time response to 2 degree perturbation in α. LOA, 120% flutter speed.	40
5.14	Frequency response. LOA, 120% flutter speed.	41

5.15 System poles and zeros. HOA, 80% flutter speed. 42
5.16 Time response to 2 degree perturbation in α. HOA, 80% flutter speed. 43
5.17 Frequency response. HOA, 80% flutter speed. 44
5.18 System poles and zeros. HOA, 120% flutter speed. 45
5.19 Time response to 2 degree perturbation in α. HOA, 120% flutter speed. 46
5.20 Frequency response. HOA, 120% flutter speed. 47
5.21 System poles and zeros. HOA, 120% flutter speed, $2 \times k_{max}$ 48
5.22 Time response to 2 degree perturbation in α. HOA, 120% flutter speed, $2 \times k_{max}$ 49
5.23 Frequency response. HOA, 120% flutter speed, $2 \times k_{max}$ 50

LIST OF TABLES

Table Number Page

2.1 Simplified equations of motion for maneuvering flexible aircraft. . . . 4

3.1 MATLAB code inputs. 19
3.2 MATLAB code outputs. Note: SS stands for State Space. 20

4.1 Physical properties of the Duke university wing/flap system. 22
4.2 Natural frequencies of the Duke university wing/flap system. 22
4.3 Flutter condition of the Duke university wing/flap system at SSL. . . 23

A.1 Poles of open and closed loop system. Perfect, 120% flutter speed. . . 56
A.2 Zeros of the system. Perfect, 120% flutter speed. 57
A.3 Poles of open and closed loop system. LOA, 120% flutter speed. . . . 57
A.4 Zeros of the system. LOA, 120% flutter speed. 58
A.5 Poles of open and closed loop system. HOA, 120% flutter speed. . . . 58
A.6 Zeros of the system. HOA, 120% flutter speed. 59

B.1 Transformed B Matrix. Perfect, 120% flutter speed. 60
B.2 Transformed C Matrix. Perfect, 120% flutter speed. 61
B.3 Transformed B Matrix. LOA, 120% flutter speed. 62
B.4 Transformed C Matrix. LOA, 120% flutter speed. 63
B.5 Transformed B Matrix. HOA, 120% flutter speed. 64
B.6 Transformed C Matrix. HOA, 120% flutter speed. 65

ACKNOWLEDGMENTS

I wish to express my sincere appreciation to Eli Livne for his immense support in creating this thesis. I am also grateful to Kristi Morgansen and the William E. Boeing Department of Aeronautics and Astronautics for their leadership throughout the program. This opportunity would not have been possible without the generosity of the National Science Foundation and the United States Air Force. Most of all, I would like to thank my wife, whose work of teaching at-risk youth inspires me on a daily basis.

DEDICATION

To my dear wife, Deborah.

Chapter 1
INTRODUCTION

1.1 Motivation

The coupling of dynamics and structural mechanics through inertial and elastic forces results in mechanical vibrations. Aeroservoelasticy studies the coupling of these mechanical vibrations with aerodynamic forces and servo dynamics on a deformable moving vehicle.[1] Such an interaction may lead to instabilities such as flutter and divergence, flutter being oscillatory in nature, and divergence being exponential.[1] Designers historically have dampened flutter by increasing the stiffness of the structure or shaping its mass distribution. But such an approach adds weight, increasing cost and hampering performance. To minimize weight, engineers commenced the development of Active Flutter Suppression (AFS). AFS makes use of control laws and dynamically activated control surfaces to suppress flutter. Boeing and Air Force engineers of the B-52 Control Configured Vehicle (CCV) program were among the first to incorporate AFS.[2] Figure 1.1 shows a modified Boeing B-52 flight testing the newly developed AFS system.[2]

The interdisciplinary reality of aeroservoelasticity increases complexity in developments, since each discipline involved defines systems in accordance with its tradition and convenience. Consequently, with structures and aerodynamic math models, information must be transferred from model to model. If time domain math models are sought, additional transformation must then be used to transfer aerodynamic data from the frequency domain, for which traditional unsteady aerodynamic models had been developed, to the time domain. Lastly, a state-space representation is developed, integrating all preceding models for control via any modern control techniques.

Figure 1.1: B-52 AFS vehicle.

1.2 Objective

The two objectives of this study were to investigate the effects of actuator math-model order and Roger approximation reduced-frequency range on Linear-Quadratic Regulator (LQR) Controlled Active Flutter Suppression (AFS).

1.3 Need

More broadly, the purpose of this project was to develop an aeroservoelastic simulation capability for open loop and closed loop systems defined by mode shapes used as generalized coordinates, generalized mass and stiffness matrices, damping, generalized aero matrices, actuators, etc., with, for exploratory studies, closing the loop by LQR control.

Chapter 2

THEORY

2.1 Equations of Motion

The work of a flight controls engineer begins with the Equations of Motion (EOM). At the onset of aviation history, mainstream developers only focused on rigid EOM, since aeroservoelastic effects were not well understood. To account for flexible effects, engineers modified rigid EOM by adding quasi-static terms.[3] However, new designs and insights brought increased attention to the field of aeroelasticity, spurring the development of more applicable flexible EOM. Unlike rigid EOM, flexible EOM have proved to be less stipulated, allowing for multiple derivations of the flexible EOM to gain acceptance by the aeroelasticians community. Quite widely used are a ZONA Technology, Inc., approach and the mean-axis approach.

The main difference between the two methods deals with how each defines the reference axes describing the motion of a free-free flexible airplane. The mean-axes serve to uncouple the rigid-body degrees of freedom and the elastic degrees of freedom by defining the axes such that the relative linear and angular momenta, due to elastic deformation, are zero at every instant.[4] This implies that the mean axes must be chosen such that:

$$\int_V \frac{\delta \bar{p}}{\delta t} \rho \, dV = \int_V \bar{p} \times \frac{\delta \bar{p}}{\delta t} \rho \, dV \tag{2.1}$$

where dV represents an infinitesimal volume at some location p with respect to the instantaneous center of mass.

The ZONA method utilizes a transformation from the principal-axes to the stability-axes.[5] In each case, the Laplace equation and the Principle of Virtual Work remain essential in deriving the EOM. The EOM derived by using the mean-axes are shown

in Table 2.1.[4]

$I_{xx}\dot{p} - (I_{xy}\dot{q} + I_{xz}\dot{r}) + (I_{zz} - I_{yy})qr + (I_{xy}r - I_{xz}q)p + (r^2 - q^2)I_{yz} = L$
$I_{yy}\dot{q} - (I_{xy}\dot{p} + I_{yz}\dot{r}) + (I_{xx} - I_{zz})pr + (I_{yz}p - I_{xy}r)q + (p^2 - r^2)I_{xz} = M$
$I_{zz}\dot{r} - (I_{xz}\dot{p} + I_{yz}\dot{q}) + (I_{yy} - I_{xx})pq + (I_{xz}q - I_{yz}p)r + (q^2 - p^2)I_{xy} = N$

Table 2.1: Simplified equations of motion for maneuvering flexible aircraft.

2.1.1 Laplace Equation

With the axis defined, the aircraft's kinetic and gravitational potential energy can be uniquely defined, leading to the total energy

$$L = KE - PE - VW \tag{2.2}$$

This equation is known as the *lagrangian*. Since the constraints of the system are holonomic, and the potential energy is a function only of independent generalized coordinates, Lagrange's equation for holonomic systems (2.3) may then be applied.[4]

$$\frac{\delta}{\delta t}(\frac{\delta L}{\delta \dot{\eta}}) - \frac{\delta L}{\delta \eta} = 0 \tag{2.3}$$

The use of Lagrangian mechanics simplifies the derivation of the EOM by allowing many of the system constraints to be bypassed.[4]

2.1.2 Principle of Virtual Work

The next step in the derivation of the flexible EOM utilizes the principle of virtual work

$$Q_i = \frac{\delta}{\delta q_i}(\delta W) \tag{2.4}$$

to determine the generalized forces, where δW is the work associated with arbitrary virtual displacements of the generalized coordinates.[4] Once the aerodynamic and

propulsive forces and moments relative to the body-reference axes are recast using virtual displacements and rotations, Equation 2.4 can be applied, completing the EOM.

2.2 Structures

Before the EOM can be used, a mathematical grid of a finite element model of the vehicle's structure must be created. An example of a structural grid created for a transport aircraft is shown in Figure 2.1.[6] The structural grid is the platform on which finite element calculations are made. These calculations provide the resulting displacements and structural forces from the input aerodynamic forces.[5] The structural grid must be generated before the modally-reduced aerodynamic model, since the generalized modal coordinates serve as the generalized coordinates used in the Langrange equation during the development of the EOM. These generalized modal coordinates are defined as

$$x = \Phi\, q \tag{2.5}$$

where Φ is a matrix containing the mode shapes of the structure found through computation or ground vibration tests. The mass, stiffness, and damping matrices are also derived during the structural portion of aerservoelastic analysis, and converted to generalized matrices:[5]

$$M = \Phi^T\, \bar{M}\, \Phi \tag{2.6}$$

$$K = \Phi^T\, \bar{K}\, \Phi \tag{2.7}$$

$$C = \Phi^T\, \bar{C}\, \Phi \tag{2.8}$$

An added advantage of using generalized coordinates is that the system can be reduced in size by only using lower frequency mode shapes. Often just a small number of the lowest natural modes is sufficient for flutter analysis of a wing.[5] Since the size of the FE matrices can be very large, then even when the number of natural modes required is large, the modal approach has the potential to greatly reduce computational cost.

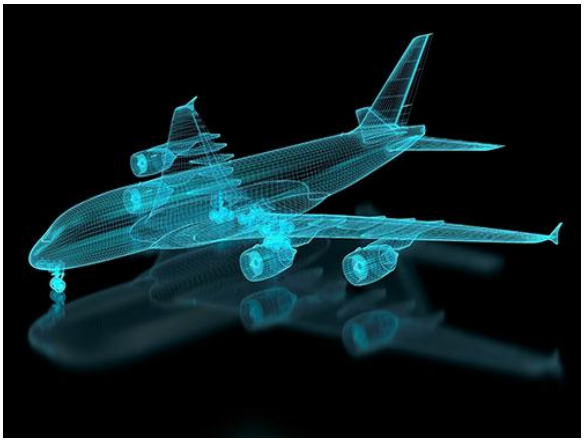

Figure 2.1: Sketch of transport aircraft FEM grid and mode shape.

It operates on the premise that the structural deformation during flutter can be sufficiently represented by the superposition of lower order modes, since critical flutter modes are usually due to the coupling of motions in the lower order structural modes.[5]

2.3 Aerodynamics

With the generalized coordinates of the vehicle defined, the generalized aerodynamic forces can be calculated. Several methods for determining linear aerodynamic forces are still used to date, the most prevalent being the doublet-lattice method, various panel methods, and strip theory.[3] Figure 2.2 represents the type of model used for panel method calculations.[5]

The key step to implementing aerodynamic forces into the aeroservoelastic system model is the creation of Aerodynamic Influence Coefficient Matrices (AIC). The AIC matrix relates local motion to local pressure distributions over the surface of a configuration.[5] The AIC matrix is then transformed to relate structural deformations to aerodynamic forces by:[5]

$$F_h = q_\infty [AIC(jk)]h \tag{2.9}$$

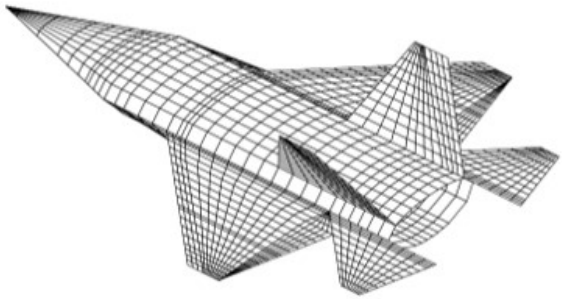

Figure 2.2: Typical Panel Model of a wing-body configuration.

where h represents the structural deformation defined at the aerodynamic boxes of the panel method, and F_h are the resultant aerodynamic forces at the aerodynamic panel due to h.[5] It is important to note that these AIC matrices depend on flight conditions, such as Mach number, and on the reduced frequency of oscillation. Therefore, a unique set of AIC matrices must be derived for each Mach number / reduced frequency pair.

2.4 Splining

As noted before, h is used to define the resultant aerodynamic forces at each aerodynamic panel. However, an additional transformation is required to transfer data between the aerodynamic panel model and the structural FE model. The transformation is completed through the process of "splining":

$$h = G\,x \tag{2.10}$$

where x are the motions of the structural FE model grid points, and G is the spline matrix. An unsteady aerodynamic code such as ZAERO, for example, uses four methods jointly to build the spline matrix, choosing each method depending on the section geometry.[5] Figure 2.3 demonstrates the spline axis along the axis of a wing-like component.[5]

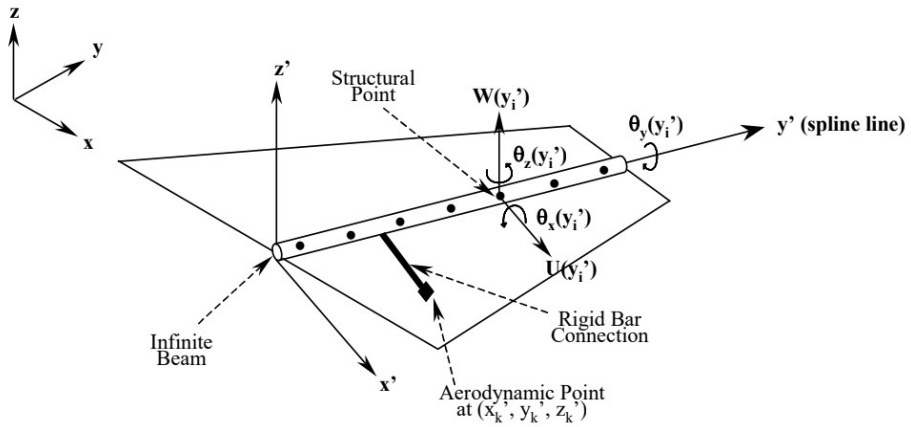

Figure 2.3: Spline axis along the axis of wing-like component.

2.5 Rational Function Approximation

Up to this point, all aerodynamic information has been transferred onto the FE model and reduced in order using some reduced order set of generalized coordinates in the form of low-frequency mode shapes. However, the AIC matrix must be recast into some form that is compatible for state-space representation. This is accomplished through a rational function approximation (RFA). There are many methods for completing the RFA, but perhaps the most known is the Roger Approximation. Keneth Roger pioneered the development of RFA for transformation AIC matrices. He knew that if he could express the AIC matrices as a Fourier Series in reduced frequency which is valid along the jw axis in the complex domain, it should be valid by analytic continuation to the left and right of the imaginary axis for values of the complex number: $s = \sigma + jw$.[1] Therefore, the Fourier transform would lead to a corresponding Laplace transform, ready for state-space representation, and if both Fourier and Laplace transforms are rational in frequency and reduced-frequency, respectively, then that would lead to Linear Time Invariant (LTI) corresponding state space models.

Roger approximated the aerodynamic matrix as a function of frequency along the

jw axis by[7]

$$A(j\omega) \approx P_0 + j\omega P_1 - \omega^2 P_2 + \frac{j\omega}{j\omega + \beta_1} P_3 + \frac{j\omega}{j\omega + \beta_2} P_4 + ... \tag{2.11}$$

where all of the P_i matrices are real and the aerodynamic lag terms β_i are real and positive. These P_i matrices and lag terms would be chosen in such a way that the approximation $A(j\omega)$ would fit the tabulated data in an optimal way. While the lag terms are chosen prior to the approximation, the P_i matrices are the calculated result of a least square approximation to the AIC matrices. But first, the dependency on jw must be converted to dependency on jk by

$$w = k\frac{U}{b} \tag{2.12}$$

since the AIC matrices are calculated using reduced frequencies, k. The resulting Roger approximation is[8]

$$A(jk) \approx \bar{P}_0 + jk\bar{P}_1 - k^2\bar{P}_2 + \frac{jk}{jk + \beta_1}\bar{P}_3 + \frac{jk}{jk + \beta_2}\bar{P}_4 + ... \tag{2.13}$$

where

$$\begin{array}{lllll} \bar{P}_0 = P_0 & \bar{P}_1 = P_1\dfrac{U}{b} & \bar{P}_2 = P_2(\dfrac{U}{b})^2 & \bar{P}_3 = P_3 & \bar{P}_4 = P_4 \quad ... \\ & & \bar{\beta}_1 = \beta_1\dfrac{U}{b} & \bar{\beta}_2 = \beta_2\dfrac{U}{b} & ... \end{array} \tag{2.14}$$

One feature of the Roger approximation that is not shared by other methods, such as the Karpel minimum-state method, is that the approximation is fitted to the tabulated aerodynamic matrices term by term at each reduced frequency.[9] Equation 2.15 demonstrates the approximation broken up term by term.

$$A(jk)_{m,n} \approx \bar{P}_{0_{m,n}} + jk\bar{P}_{1_{m,n}} - k^2\bar{P}_{2_{m,n}} + \frac{jk}{jk + \beta_1}\bar{P}_{3_{m,n}} + \frac{jk}{jk + \beta_2}\bar{P}_{4_{m,n}} + ... \tag{2.15}$$

As a preceding step to solving for the P matrices, the rational functions in the approximation must be separated into real and imaginary parts, as shown in Equation 2.16.[8]

$$\frac{jk}{jk + \bar{\beta}_1} = \frac{k^2 + jk\bar{\beta}_1}{k^2 + {\bar{\beta}_1}^2} = \frac{k^2}{k^2 + {\bar{\beta}_1}^2} + \frac{jk\bar{\beta}_1}{k^2 + {\bar{\beta}_1}^2} \tag{2.16}$$

The least squares approximation seeks to minimize the sum of the squares of the errors between the actual data and the approximation at each reduced frequency. To guarantee a perfect match between the AIC matrix and the approximation at $k_0 = 0$, which is the steady state solution, we set

$$\bar{P}_0 = A(k = 0) \tag{2.17}$$

Making use of Equation 2.16, and using two aerodynamic lag roots, the approximation separated into real and imaginary parts is[8]

$$\begin{bmatrix} 0 & -{k_1}^2 & \frac{{k_1}^2}{{k_1}^2+\bar{\beta_1}^2} & \frac{{k_1}^2}{{k_1}^2+\bar{\beta_2}^2} \\ k_1 & 0 & \frac{k_1\bar{\beta_1}}{{k_1}^2+\bar{\beta_1}^2} & \frac{k_1\bar{\beta_2}}{{k_1}^2+\bar{\beta_2}^2} \\ \vdots & \vdots & \vdots & \vdots \\ 0 & -{k_N}^2 & \frac{{k_N}^2}{{k_N}^2+\bar{\beta_1}^2} & \frac{{k_N}^2}{{k_N}^2+\bar{\beta_2}^2} \\ k_N & 0 & \frac{k_N\bar{\beta_1}}{{k_N}^2+\bar{\beta_1}^2} & \frac{k_N\bar{\beta_2}}{{k_N}^2+\bar{\beta_2}^2} \end{bmatrix} \begin{bmatrix} P_{1_{m,n}} \\ P_{2_{m,n}} \\ P_{3_{m,n}} \\ P_{4_{m,n}} \end{bmatrix} \approx \begin{bmatrix} Re(A_{m,n}(jk_1)) - A_{m,n}(k_0 = 0) \\ Im(A_{m,n}(jk_1)) \\ \vdots \\ Re(A_{m,n}(jk_N)) - A_{m,n}(k_0 = 0) \\ Im(A_{m,n}(jk_N)) \end{bmatrix} \tag{2.18}$$

which matches the least squares form of

$$L\{x\} \approx R \tag{2.19}$$

Using least squares approximation on Equation 2.18, the terms

$$\{x\} = \begin{bmatrix} P_{1_{m,n}} \\ P_{2_{m,n}} \\ P_{3_{m,n}} \\ P_{4_{m,n}} \end{bmatrix} \tag{2.20}$$

are found. With a given speed, U, and flight atmospheric density, ρ, the P_i and β_i terms can be found from $\bar{P}_i$ and $\bar{\beta}_i$:

$$\begin{array}{lllll} P_0 = \bar{P}_0 & P_1 = \bar{P}_1\dfrac{b}{U} & P_2 = \bar{P}_2\dfrac{b}{U}^2 & P_3 = \bar{P}_3 & P_4 = \bar{P}_4 \quad ... \\ & & \beta_1 = \bar{\beta}_1\dfrac{b}{U} & \beta_2 = \bar{\beta}_2\dfrac{b}{U} & ... \end{array} \tag{2.21}$$

The Roger approximated AIC matrices can then be used to generate state space models.

As stated in the objectives, in this study we hoped to learn how the Roger approximation frequency range affects generated LQR control. The Roger approximation is based on k frequencies up to some k_{max}. As a result, there is a limit of validity of the time domain to model real frequencies, up to:

$$\omega_{max} = k_{max}\frac{U}{b} \tag{2.22}$$

Therefore, it was important to learn what effect this has on the LQR-based closed loop control that "does not know" that the plant model is only valid up to ω_{max}.

2.6 State-Space Representation

As most modern control techniques utilize state-space representation, the obvious last step is to integrate all elements into a state-space representation. The plant and actuator representation must first be independently formulated before being combined to an overall system representation.

2.6.1 Plant

The derivation of the plant state-space representation begins with the EOM of the aeroservoelastic system based on the equilibrium of forces:

$$Ms^2\{q\} + Cs\{q\} + K\{q\} - q_D A(s)\{q\} = \{0\} \tag{2.23}$$

where M and K are the mass and stiffness matrices generated by the structural FE method, and C is the damping matrix. For this study, all external forces were excluded, except for the aerodynamic forces due to elastic deformation. The model of the system was limited to focus on the response to imposed control effector motions.

Inserting the Roger approximation of the generalized AIC in the Laplace domain,

Equation 2.23 becomes (using two Roger lag terms)

$$Ms^2\{q\}+Cs\{q\}+K\{q\}-q_D[P_0+sP_1+s^2P_2+\frac{s}{s+\beta_1}P_3+\frac{s}{s+\beta_2}P_4]\{q\}=\{0\} \quad (2.24)$$

Equations 2.25, 2.26, and 2.27, shown with all matrices partitioned into structural and/or control related terms, combine the mass, damping, and stiffness matrices with dynamic pressure and the P_i terms.[10]

$$\begin{bmatrix}\bar{M}_{ss} & \bar{M}_{sc}\\ \bar{M}_{cs} & \bar{M}_{cc}\end{bmatrix}=\begin{bmatrix}M_{ss} & M_{sc}\\ M_{cs} & M_{cc}\end{bmatrix}-q_D\begin{bmatrix}P_{2_{ss}} & P_{2_{sc}}\\ P_{2_{cs}} & P_{2_{cc}}\end{bmatrix} \quad (2.25)$$

$$\begin{bmatrix}\bar{C}_{ss} & \bar{C}_{sc}\\ \bar{C}_{cs} & \bar{C}_{cc}\end{bmatrix}=\begin{bmatrix}C_{ss} & C_{sc}\\ C_{cs} & C_{cc}\end{bmatrix}-q_D\begin{bmatrix}P_{1_{ss}} & P_{1_{sc}}\\ P_{1_{cs}} & P_{1_{cc}}\end{bmatrix} \quad (2.26)$$

$$\begin{bmatrix}\bar{K}_{ss} & \bar{K}_{sc}\\ \bar{K}_{cs} & \bar{K}_{cc}\end{bmatrix}=\begin{bmatrix}K_{ss} & K_{sc}\\ K_{cs} & K_{cc}\end{bmatrix}-q_D\begin{bmatrix}P_{0_{ss}} & P_{0_{sc}}\\ P_{0_{cs}} & P_{0_{cc}}\end{bmatrix} \quad (2.27)$$

The generalized deformation q can likewise be separated into structural deformation and controlled control surface motions by

$$\{q(s)\}=\begin{Bmatrix}q_s(s)\\ q_c(s)\end{Bmatrix} \quad (2.28)$$

After inserting Equations 2.25, 2.26, 2.27, and 2.28, and, focusing on the system response to imposed control effector motions, the upper partition of Equation 2.24 becomes[10]

$$\begin{aligned}&\bar{M}_{ss}s^2q_s+\bar{C}_{ss}sq_s+\bar{K}_{ss}q_s-q_D[P_{3_{ss}}\quad P_{3_{sc}}]\frac{s}{s+\beta_1}\begin{Bmatrix}q_s\\ q_c\end{Bmatrix}\\ -...&q_D[P_{2+N_{L_{ss}}}\quad P_{2+N_{L_{sc}}}]\frac{s}{s+\beta_{N_L}}\begin{Bmatrix}q_s\\ q_c\end{Bmatrix}=-\bar{M}_{sc}s^2q_c-\bar{C}_{sc}sq_c-\bar{K}_{sc}q_c\end{aligned} \quad (2.29)$$

The states are then defined as:

$$\begin{aligned}
\{x_1\} &= \{q_s\} \\
\{x_2\} &= s\{q_s\} = s\{x_1\} \\
&\frac{s}{s+\beta_1}\begin{Bmatrix} q_s \\ q_c \end{Bmatrix} = \{r_1\} \\
&\vdots \\
&\frac{s}{s+\beta_{N_L}}\begin{Bmatrix} q_s \\ q_c \end{Bmatrix} = \{r_{N_L}\}.
\end{aligned} \tag{2.30}$$

Inserting the defined states, Equation 2.29 become

$$\begin{aligned}
&\bar{M}_{ss}s\{x_2\} + \bar{C}_{ss}\{x_2\} + \bar{K}_{ss}\{x_1\} - q_D[P_{3_{ss}} \quad P_{3_{sc}}]\{r_1\} \\
&- ...q_D[P_{2+N_{L\,ss}} \quad P_{2+N_{L\,sc}}]\{r_{N_L}\} = -[\bar{K}_{sc} \quad -\bar{C}_{sc} \quad -\bar{M}_{sc}]\begin{Bmatrix} q_c \\ sq_c \\ s^2q_c \end{Bmatrix}
\end{aligned} \tag{2.31}$$

which solved for $s\{x_2\}$ is

$$\begin{aligned}
s\{x_2\} &= -\bar{M_{ss}}^{-1}\bar{K}_{ss}\{x_1\} - \bar{M_{ss}}^{-1}\bar{C}_{ss}\{x_2\} + q_D\bar{M_{ss}}^{-1}[P_{3_{ss}} \quad P_{3_{sc}}]\{r_1\} \\
&+ ...q_D\bar{M_{ss}}^{-1}[P_{2+N_{L\,ss}} \quad P_{2+N_{L\,sc}}]\{r_{N_L}\} = -\bar{M_{ss}}^{-1}[-\bar{K_{sc}} \quad -\bar{C_{sc}} \quad -\bar{M}_{sc}]\begin{Bmatrix} q_c \\ sq_c \\ s^2q_c \end{Bmatrix}
\end{aligned} \tag{2.32}$$

Further refining the formulation, the lag states can be expressed as[10]

$$\begin{aligned}
s\{r_1\} = -\beta_1\{r_1\} + s\begin{Bmatrix} q_s \\ q_c \end{Bmatrix} &= -\beta_1\{r_1\} + \begin{bmatrix} 1 \\ 0 \end{bmatrix}\{x_2\} + \begin{bmatrix} 0 & 0 & 0 \\ 0 & 1 & 0 \end{bmatrix}\begin{Bmatrix} q_c \\ sq_c \\ s^2q_c \end{Bmatrix} \\
&= -\beta_1\{r_1\} + [R_x]\{x_2\} + [R_c]\begin{Bmatrix} q_c \\ sq_c \\ s^2q_c \end{Bmatrix}
\end{aligned} \tag{2.33}$$

Together this yields a state vector of the aeroservoelastic plant of

$$\{x_p\} = \begin{Bmatrix} \{x_1\} \\ \{x_2\} \\ \{r_1\} \\ \vdots \\ \{r_{N_L}\} \end{Bmatrix} \tag{2.34}$$

and an input vector of

$$\{u_{p_c}\} = \begin{Bmatrix} q_c \\ sq_c \\ s^2 q_c \end{Bmatrix} \tag{2.35}$$

With these states, the plant matrix becomes[10]

$$A_p = \begin{bmatrix} 0 & I & 0 & ... & 0 \\ A_{p_{(2,1)}} & A_{p_{(2,2)}} & A_{p_{(2,3)}} & ... & A_{p_{(2,2+N_L)}} \\ 0 & R_x & -\beta\, I & ... & 0 \\ \vdots & \vdots & \vdots & \vdots & \vdots \\ 0 & R_x & 0 & ... & -\beta_{N_L}\, I \end{bmatrix} \tag{2.36}$$

$$B_p = \begin{bmatrix} 0 \\ \bar{M_{ss}}^{-1}[-\bar{K_{sc}} \quad -\bar{C_{sc}} \quad -\bar{M_{sc}}] \\ R_c \\ \vdots \\ R_C \\ 0 \\ 0 \\ 0 \end{bmatrix}. \tag{2.37}$$

where

$$\begin{gathered} A_{p_{(2,1)}} = -\bar{M_{ss}}^{-1}\bar{K_{ss}} \qquad A_{p_{(2,2)}} = -\bar{M_{ss}}^{-1}\bar{C_{ss}} \\ A_{p_{(2,3)}} = q_D \bar{M_{ss}}^{-1}[P_{3_{ss}} \quad P_{3_{sc}}] \qquad A_{p_{(2,2+N_L)}} = q_D \bar{M_{ss}}^{-1}[P_{2+N_{L\,ss}} \quad P_{2+N_{L\,sc}}] \end{gathered} \tag{2.38}$$

and

$$s\{x_p\} = A_p\{x_p\} + B_p\{u_p\} \tag{2.39}$$

The aeroservoelastic plant outputs are more conveniently understood by the displacements, velocities, and accelerations at a small set of nodes. Since the states of the system are expressed in generalized coordinates, they must be transformed. The transformation from generalized coordinates is given by Equation 2.5. We can then use transformation matrices T_d, T_v, T_a made of zeros and ones to project the full sets of displacements, velocities, and accelerations onto just those were they are measured by sensors.[10] This dual transformation is shown in Equation 2.40.

$$\{y_p\} = T_d\Phi\{q_s\} + T_v\Phi s\{q_s\} + T_a\Phi s^2\{q_s\} \tag{2.40}$$

Since $\{q_s\}$ is a subset of the states of the aeroelastic plant $\{x_p\}$, they can be extracted via

$$\{q_s\} = [I \quad 0 \quad 0 \quad ... \quad 0]\{x_p\} = T_{sp}\{x_p\} \tag{2.41}$$

Equation 2.40 may then be expressed as[10]

$$\{y_p\} = T_d\Phi T_{sp}\{x_p\} + T_v\Phi s T_{sp}\{x_p\} + T_a\Phi s^2 T_{sp}\{x_p\} \tag{2.42}$$

Now, $\{x_p\}$ and $s\{x_p\}$ have previously been derived in state-space form, so $s^2\{x_p\}$ can be found by

$$s^2\{x_p\} = A_p s\{x_p\} + B_p s\{u_p\} = {A_p}^2\{x_p\} + A_p B_p s\{u_p\} + B_p s\{u_p\} \tag{2.43}$$

Using Equation 2.39 and 2.43 in 2.42 yields[10]

$$\{y_p\} = C_p\{x_p\} + D_p\{u_p\} + \bar{D}_p s\{u_p\} \tag{2.44}$$

where

$$C_p = [T_d\Phi T_{sp} + T_v\Phi T_{sp}A_p + T_a\Phi T_{sp}{A_p}^2] \tag{2.45}$$

$$D_p = [T_v\Phi T_{sp}B_p + T_a\Phi T_{sp}A_p B_p] \tag{2.46}$$

$$\bar{D}_p = [T_a\Phi T_{sp}B_p] \tag{2.47}$$

2.6.2 Actuator

For a single actuator described by a strictly proper transfer function, its output is the forced motion of a control surface described by[10]

$$s\{x_a\} = A_a\{x_a\} + \{B_a\}\{u_a\} \tag{2.48}$$

$$\{q_c\} = \{y_a\} = \{C_a\}\{x_a\} \tag{2.49}$$

The higher order derivatives of control surface motions are thus:

$$s\{q_c\} = s\{C_a\}A_a\{x_a\} + \{C_a\}\{B_a\}\{u_a\} \tag{2.50}$$

and

$$s^2\{q_c\} = \{C_a\}{A_a}^2\{x_a\} + \{C_a\}A_a\{B_a\}\{u_a\} + \{C_a\}\{B_a\}s\{u_a\} \tag{2.51}$$

When the order of the denominator of the actuator transfer function is two order greater than the order of the numerator, then, in Equation 2.51:[10]

$$\{C_a\}\{B_a\} = 0 \tag{2.52}$$

When the order of the denominator of the actuator transfer function is more than two order greater than the order of the numerator, then, in Equation 2.51:[10]

$$\{C_a\}A_a\{B_a\} = 0 \tag{2.53}$$

For the prior case, the equations that relate actuator outputs to its inputs are given by Equation 2.48 and:

$$\{y_a\} = \begin{Bmatrix} q_c \\ sq_c \\ s^2q_c \end{Bmatrix} = \begin{Bmatrix} \{C_a\} \\ \{C_a\}A_a \\ \{C_a\}{A_a}^2 + \{C_a\}A_a\{B_a\} \end{Bmatrix} = \{C_A\}\{x_a\}. \tag{2.54}$$

For the later case:

$$\{y_a\} = \begin{Bmatrix} q_c \\ sq_c \\ s^2q_c \end{Bmatrix} = \begin{Bmatrix} \{C_a\} \\ \{C_a\}A_a \\ \{C_a\}{A_a}^2 \end{Bmatrix} = \{C_A\}\{x_a\}. \tag{2.55}$$

2.6.3 The Integrated System

The input of the aeroelastic plant is the output from the actuator:

$$\{u_p\} = \{y_a\} = C_A\{x_a\} \tag{2.56}$$

The last term of the aeroelastic plant output $s\{u_p\}$ can be found from Equations 2.55 and 2.56:

$$s\{u_p\} = C_A A_a\{x_a\} + C_A\{B_a\}u_a \tag{2.57}$$

The input equations are

$$\begin{aligned} s\{x_p\} &= A_p\{x_p\} + B_p C_A\{x_a\} \\ s\{x_a\} &= A_a\{x_a\} + \{B_a\}u_a \end{aligned} \tag{2.58}$$

The output equations are

$$\begin{aligned} \{y_p\} &= C_p\{x_p\} + D_p C_A\{x_a\} + \bar{D}_p C_A A_a\{x_a\} + \bar{D}_p C_A\{B_a\}u_a \\ \{y_a\} &= C_A\{x_a\} \end{aligned} \tag{2.59}$$

In matrix form, the complete system becomes[10]

$$s\begin{Bmatrix} x_p \\ x_a \end{Bmatrix} = \begin{bmatrix} A_p & B_p C_A \\ 0 & A_a \end{bmatrix}\begin{Bmatrix} x_p \\ x_a \end{Bmatrix} + \begin{bmatrix} \{0\} \\ \{B_a\} \end{bmatrix} u_a \tag{2.60}$$

$$\begin{Bmatrix} y_p \\ y_a \end{Bmatrix} = \begin{bmatrix} C_p & D_p C_A + \bar{D}_p C_A A_a \\ 0 & C_A \end{bmatrix}\begin{Bmatrix} x_p \\ x_a \end{Bmatrix} + \begin{bmatrix} \bar{D}_p C_A\{B_a\} \\ \{0\} \end{bmatrix} u_a \tag{2.61}$$

To close the system, an LQR controller was used. The LQR uses a gain matrix K found using the Ricatti equation which shifts the poles of the system to the negative plane by

$$A_{sys-closed} = A_{sys} - B_{sys}K \tag{2.62}$$

Equation 2.62 is then inserted into the system to give a new state-space system of

$$s\{x\} = A_{sys-closed}\{x\} + B_{sys}u_a \tag{2.63}$$

$$y_{sys} = C_{sys}\{x\} + D_{sys}u_a \tag{2.64}$$

Note that in full-state LQR control the output equation of the system is not used in the feedback loop.

Chapter 3

MATLAB CODE DESCRIPTION

The MATLAB code developed takes the inputs shown in Table 3.1, and provides the outputs shown in Table 3.2.

M	Mass matrix
K	Stiffness matrix
C	Damping matrix
AIC	Aerodynamic influence coefficient matrix
Φ	Mode shapes
ρ	Density
b	Reference length
ns/nc	Number of structural/control DOF
k	Reduced frequencies
b_lag	Lag terms
W	Roger weighting matrix
sensor_dof_d/v/a	Node number of displacement/velocity/acceleration sensor
A/B/C/D_act	Actuator dynamics
U_max	Max velocity
w_max	Max frequency
Q,R	LQR weighting
x0	Initial condition for time response

Table 3.1: MATLAB code inputs.

The MATLAB code flowchart is shown in Fig 3.1. As shown, the code utilizes four external functions.

sys	Open_loop SS system
sys_cl	Closed_loop SS system
U_flutter	Flutter speed
w_flutter	Flutter frequency
uc/uo	Uncontrollable/Unobservable state number
B/Ctilde	Transformed B/C matrices
w_n	Natural frequency
e_real/imag_avg	Roger approximation avg. real/imag.error

Table 3.2: MATLAB code outputs. Note: SS stands for State Space.

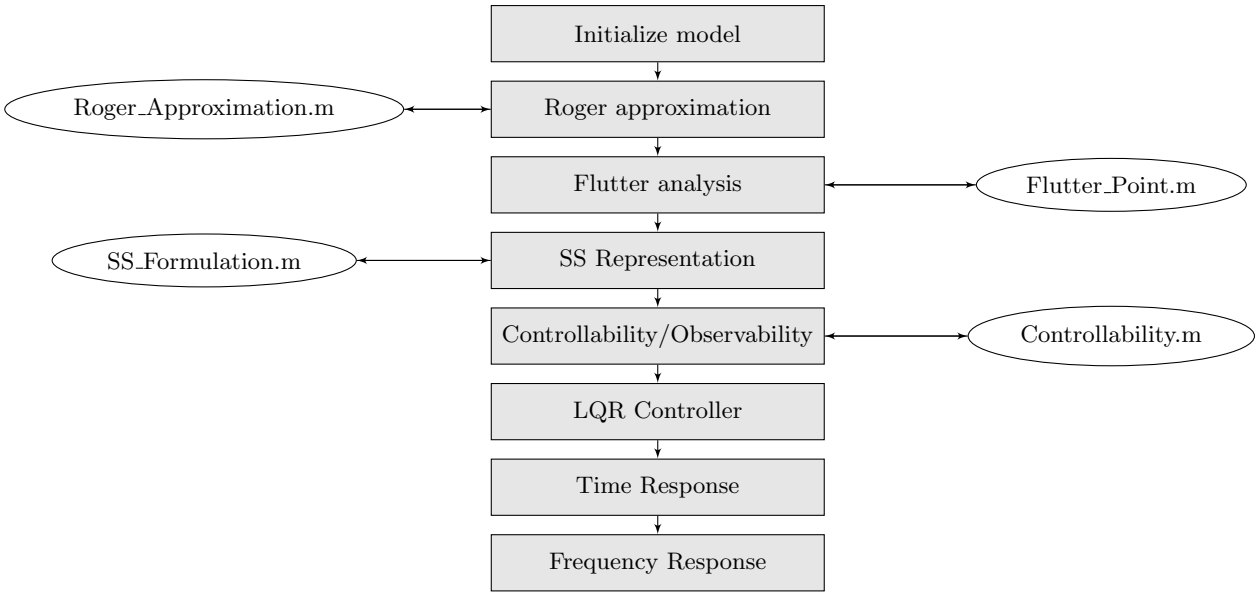

Figure 3.1: MATLAB code flowchart.

Chapter 4

TEST SYSTEM DESCRIPTION

4.1 Duke University wing/flap system

For this study, the Duke University wing/flap system was used, which is depicted in Figure 4.1.[11] The span was sufficiently long and extended from floor to ceiling of the test section. The cross-section could be, therefore, studied as two-dimensional. The system has three degrees-of-freedom: hinge rotation, system rotation, and system plunge displacement. Stiffness was incorporated using torsional and linear springs. The physical properties of the system are shown in Table 4.1[11]

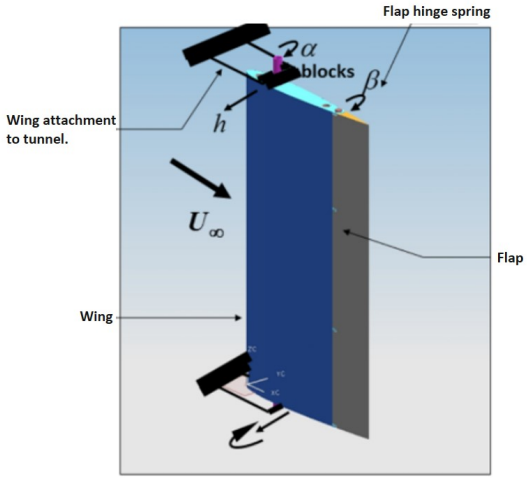

Figure 4.1: Duke University wing/flap system design.

The natural frequencies of the system ω_N were found from the free vibration problem using M and K, the mass and stiffness matrices. The comparison of the measured and predicted natural frequencies is shown in Table 4.2.

chord	0.254 m
Elastic axis	0.64 m
Hinge line	0.191 m
Mass/span	1.558 kg/m
S_α	0.08587 kg m/m
S_β	0.00395 kg m/m
I_α	0.01347 kg m^2/m
I_β	0.0003246 kg m^2/m
K_α	37.34 kg N/rad
K_h	2818.4 kg N/m/m
K_β	3.895 kg N/rad

Table 4.1: Physical properties of the Duke university wing/flap system.

Measured[11] (Hz)		
4.375	9.125	18.625
Predicted (Hz)		
4.455	9.220	19.476

Table 4.2: Natural frequencies of the Duke university wing/flap system.

The flutter speed and frequency was determined using a root locus method. The speed of the system was increased until the eigenvalues of the plant crossed the real axis. The system was evaluated at Sea-Level Standard Day (SSD) conditions. The comparison of the measured and predicted flutter condition is shown in Table 4.3.

The modes of the system were calculated using the eigenvectors of the free vibra-

$U_{flutter}$	$\omega_{flutter}$
Measured[11]	
20.6 m/s	5.47 Hz
Predicted	
24.0 m/s	6.06 Hz

Table 4.3: Flutter condition of the Duke university wing/flap system at SSL.

tion problem. A control mode shape was incorporated by adding a fourth column with a unit value correlating to hinge rotation. The results are shown in Equation 4.1.

$$\Phi = \begin{bmatrix} 0.504 & -0.308 & 0.056 & 0 \\ 1.282 & 8.763 & -4.977 & 0 \\ 0.656 & 7.207 & 59.861 & 1 \end{bmatrix} \tag{4.1}$$

Two sensors were simulated for this study, one at the leading edge, and one at the hinge line. Figure 4.2 depicts the location of the sensors. The sensors were assumed to be perfect, so no sensor dynamics were included.

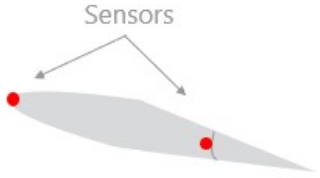

Figure 4.2: Sensor placement on wing/flap system.

4.2 Actuators

Three actuator cases were used for this study. The first actuator case assumed a perfect irreversible actuator. Thus no actuator dynamics were included. The state-space representation found in Section 2.6 was edited by omitting the second rows and columns of the symbolic state-space representation.

The remaining actuator cases used a Low-Order Actuator (LOA) or a High-Order Actuator (HOA) transfer function found in the report of an F/A-18 test vehicle, shown in Figure 4.3.[12] Note: the intention here is not to simulate actuators that may be applied to the very simple Duke system, but to examine the effect of model order of some physical actuators on the dynamics and control of the system.

Figure 4.3: F/A-18 HARV TVCS aircraft in flight.

The LOA transfer function is[12]

$$\frac{75^2}{s^2 + 2(0.59)(75)s + (75)^2} \tag{4.2}$$

The HOA transfer function is[12]

$$\begin{aligned}(2.0 \times 10^{16})&\frac{s + 356}{[s^2 + 2(.62)(69.1)s + (69.1)^2]} \\ \times &\frac{1}{[s^2 + 2(.94)(392)s + (392)^2][s^2 + 2(.82)(746)s + (746)^2](s + 718)]}\end{aligned} \tag{4.3}$$

Since the numerator of the LOA is not more than two order greater than the denominator, the state space representation found in Section 2.6 was edited by including $\{C_a\}A_a\{B_a\}$ into the third row of C_A. That is:

$$C_A = \begin{Bmatrix} \{C_a\} \\ \{C_a\}A_a \\ \{C_a\}{A_a}^2 + \{C_a\}A_a\{B_a\} \end{Bmatrix} \tag{4.4}$$

The frequency response plots for the three actuator outputs are shown in Figures 4.4, 4.5, and 4.6.

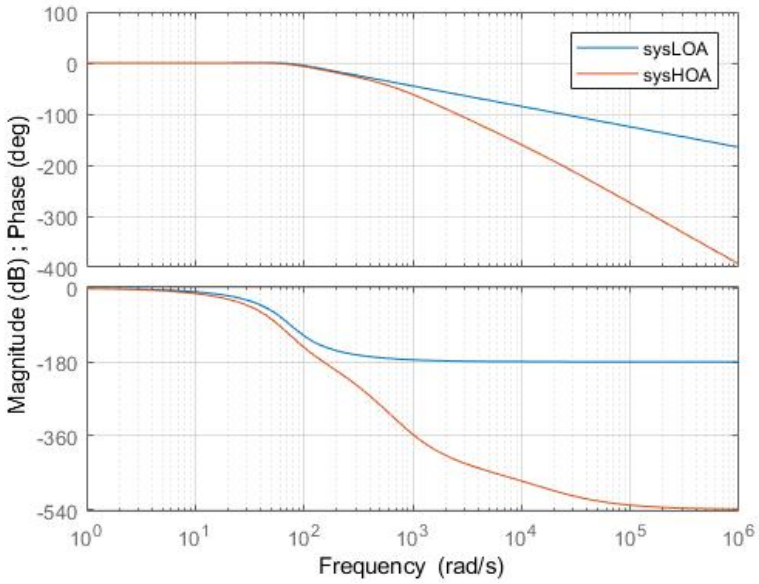

Figure 4.4: Actuator comparison Bode plots - Output q_c.

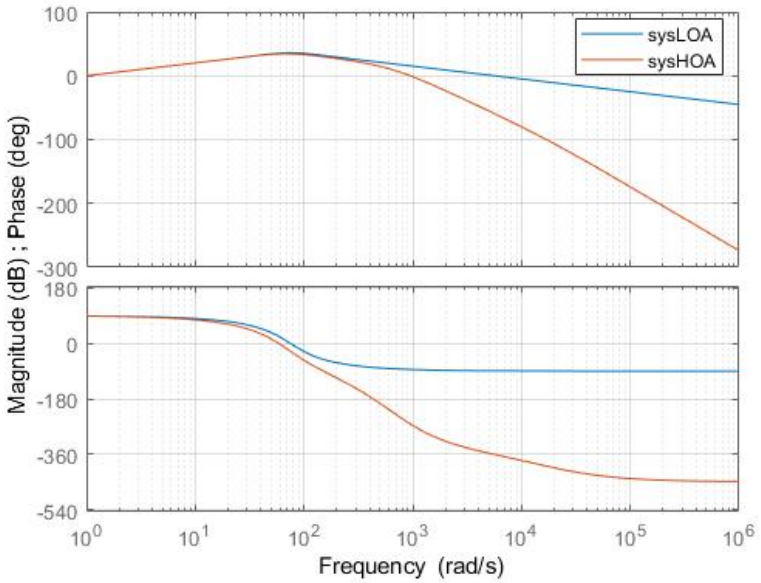

Figure 4.5: Actuator comparison Bode plots - Output sq_c.

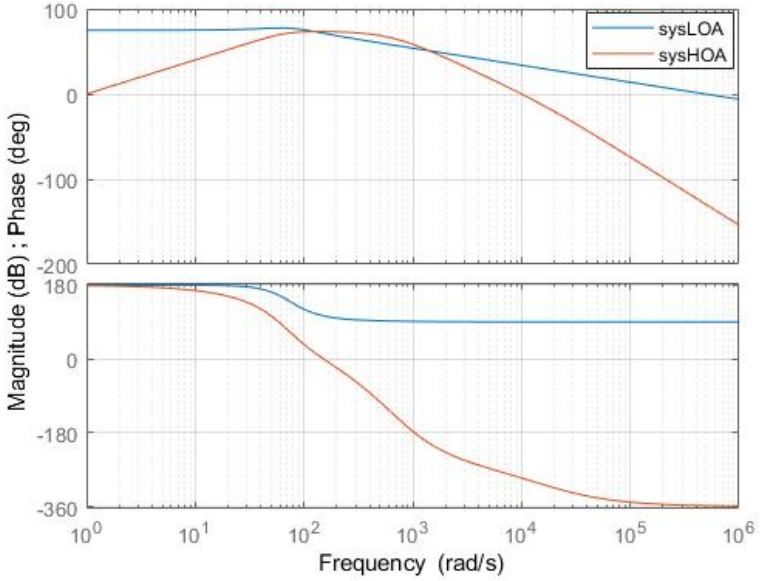

Figure 4.6: Actuator comparison Bode plots - Output s^2q_c.

Chapter 5

RESULTS

Seven cases were run for this study. Open and closed loop responses were determined at 80% and 120% flutter speed for each of the three actuators. Each simulation was run at SSD conditions, with the reduced frequencies and aerodynamic lag terms shown in Equation 5.1.

$$\begin{aligned} k_1 &= [0\ 0.05\ 0.1\ 0.2\ 0.3\ 0.4\ 0.5\ 0.7\ 0.9\ 1.1\ 1.4\ 1.7\ 2.0\ 2.5\ 3.0] \\ \beta_1 &= [0.3\ 0.8] \end{aligned} \tag{5.1}$$

An additional case was run for the HOA with the values shown in Equation 5.2 at 120% flutter speed.

$$\begin{aligned} k_2 &= [0\ 0.05\ 0.1\ 0.2\ 0.3\ 0.4\ 0.5\ 0.7\ 0.9\ 1.1\ 1.4\ 1.7\ 2.0 \\ &\quad\ 2.5\ 3.0\ 3.5\ 4\ 4.5\ 5\ 5.5\ 6] \\ \beta_2 &= [0.3\ 0.8\ 1] \end{aligned} \tag{5.2}$$

The Roger approximation had an error of 3.2% for imaginary values and 0.4% for real values. By increasing the k_{max} and adding another lag term, the error was reduced to 1.7% for imaginary values and 0.2% for real values. The comparisons for both cases are shown in Figure 5.1 and 5.2.

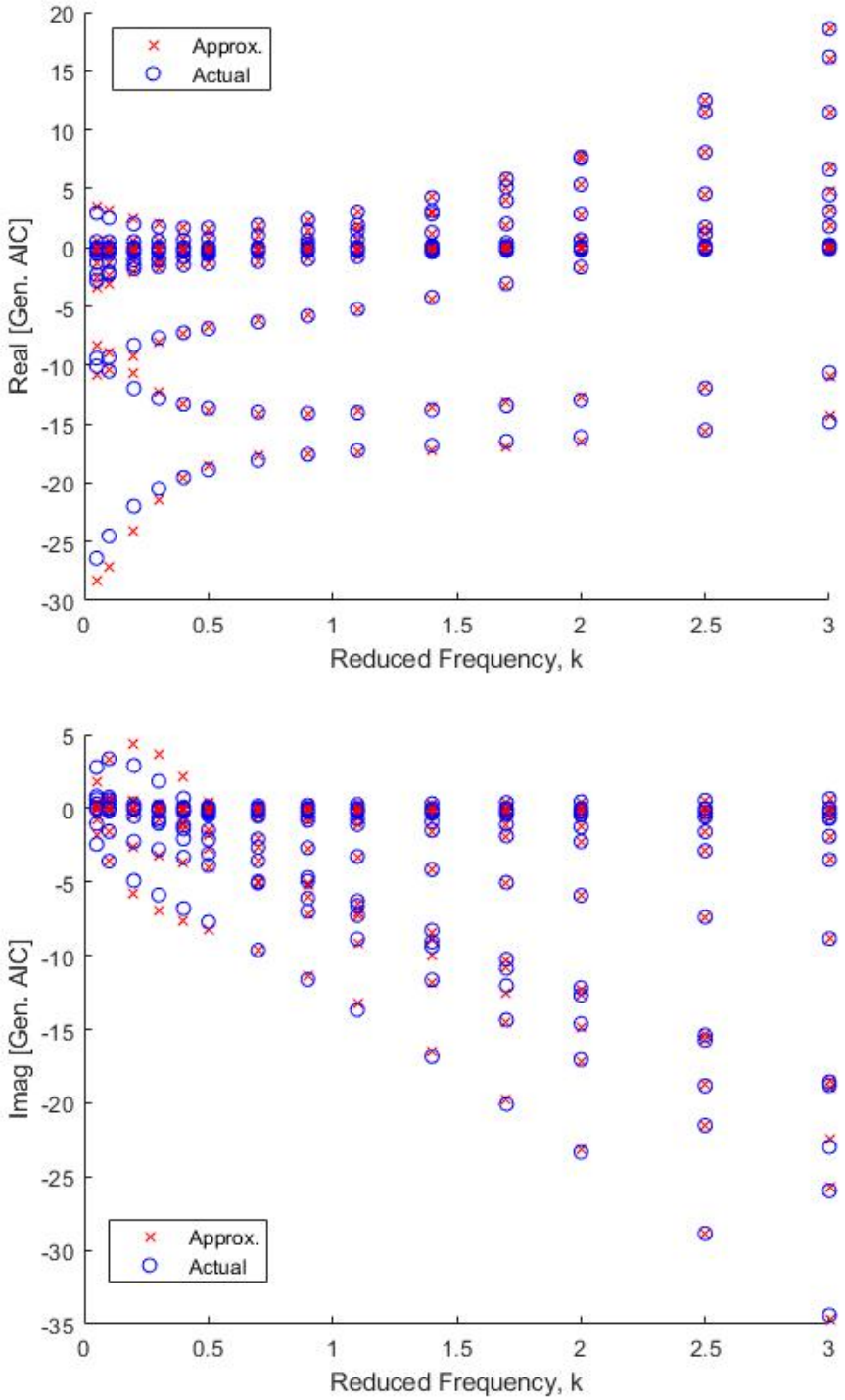

Figure 5.1: Roger approximation comparison to actual data. Perfect, k_{set1}

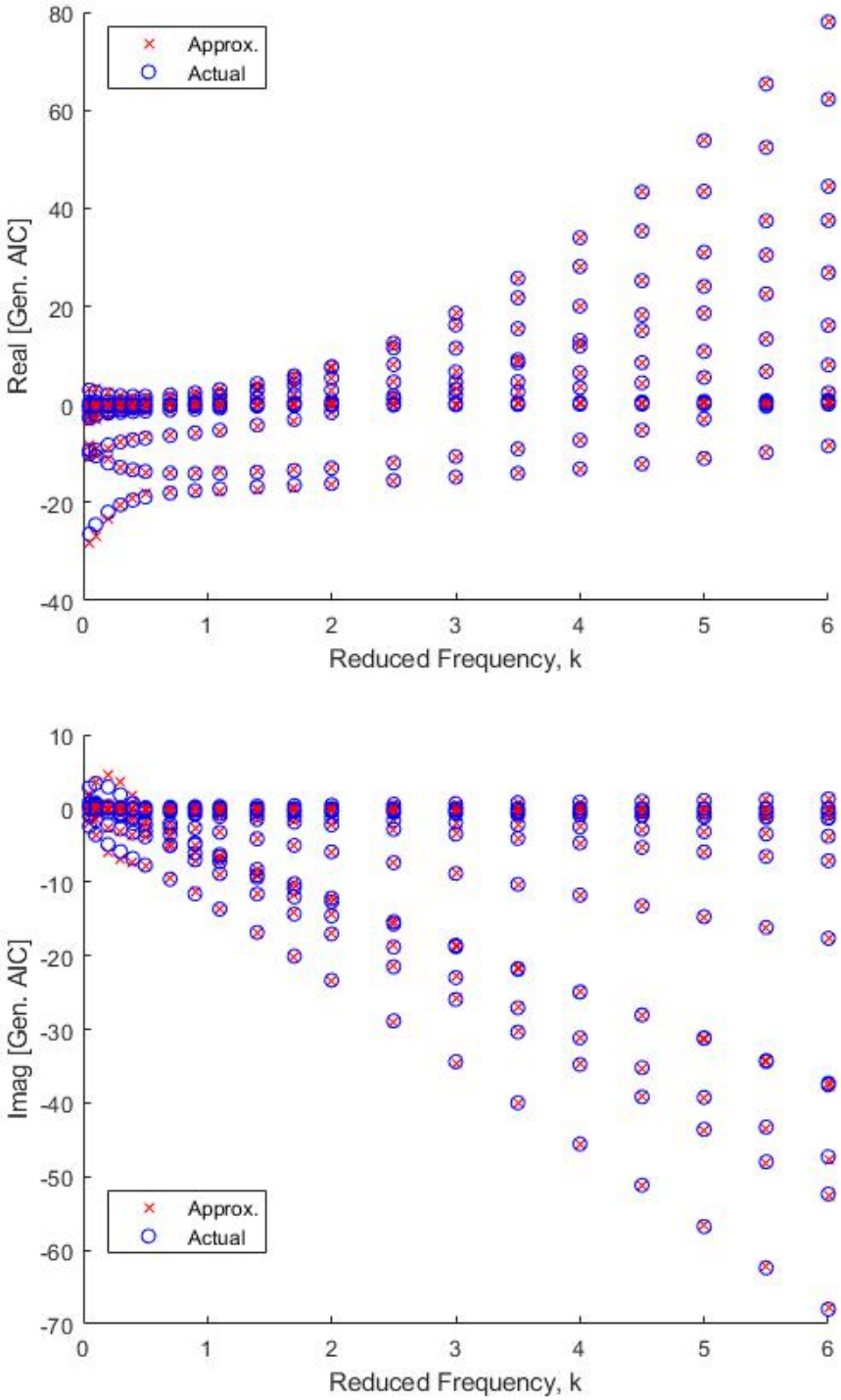

Figure 5.2: Roger approximation comparison to actual data. Perfect, k_{set2}

5.1 Case 1 : Perfect Actuator - 80% *Flutter*

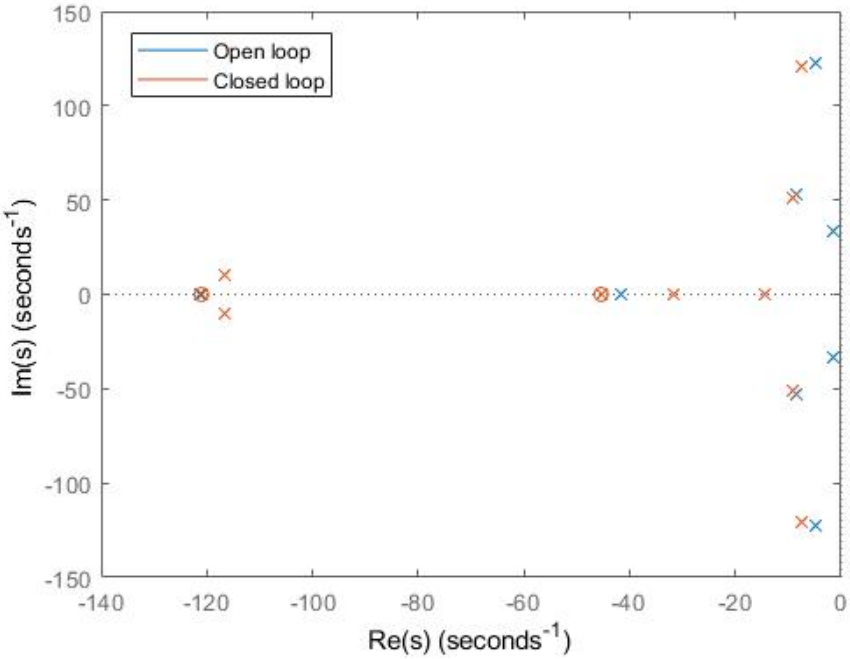

Figure 5.3: System poles and zeros. Perfect, 80% flutter speed.

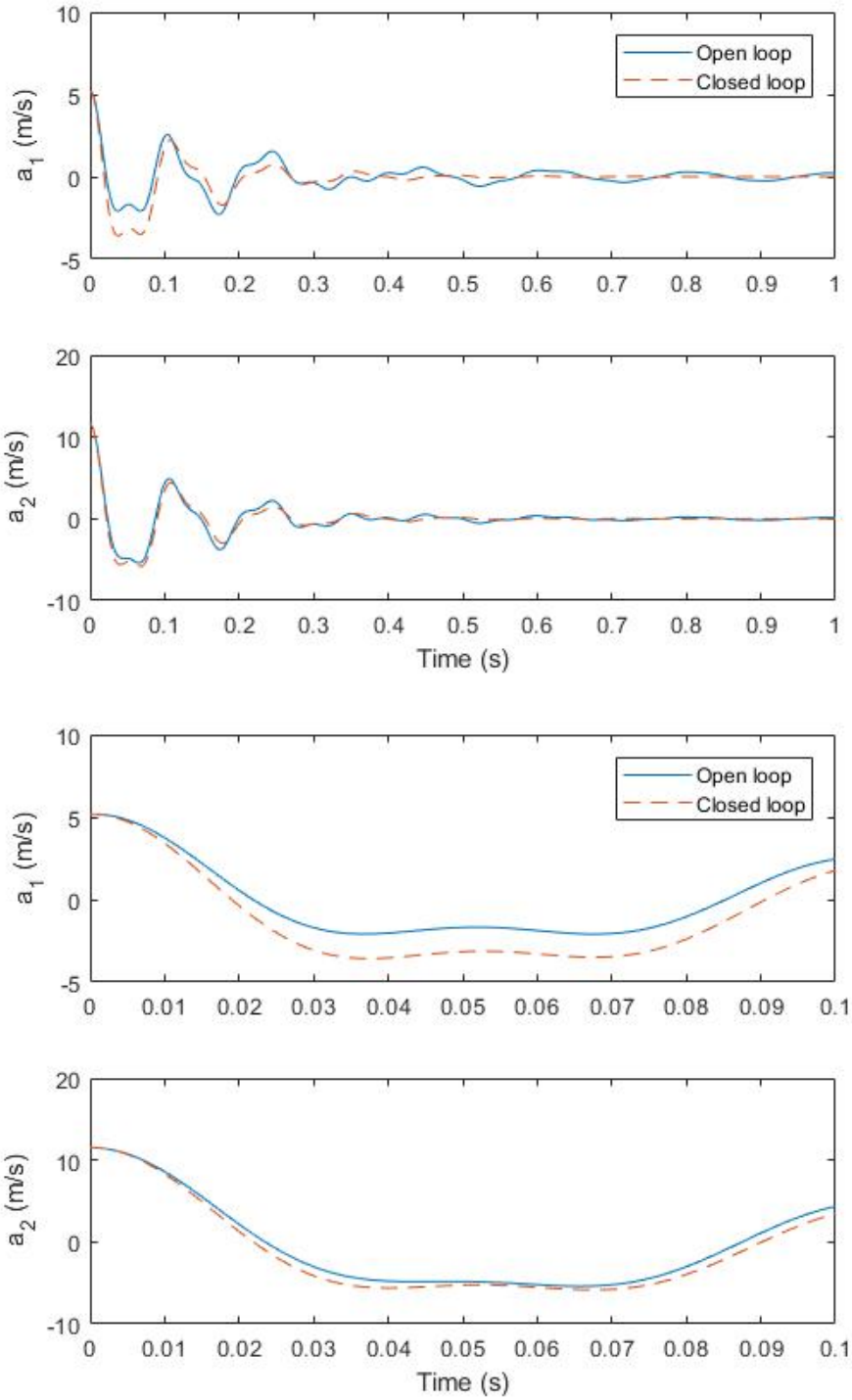

Figure 5.4: Time response to 2 degree perturbation in α. Perfect, 80% flutter speed.

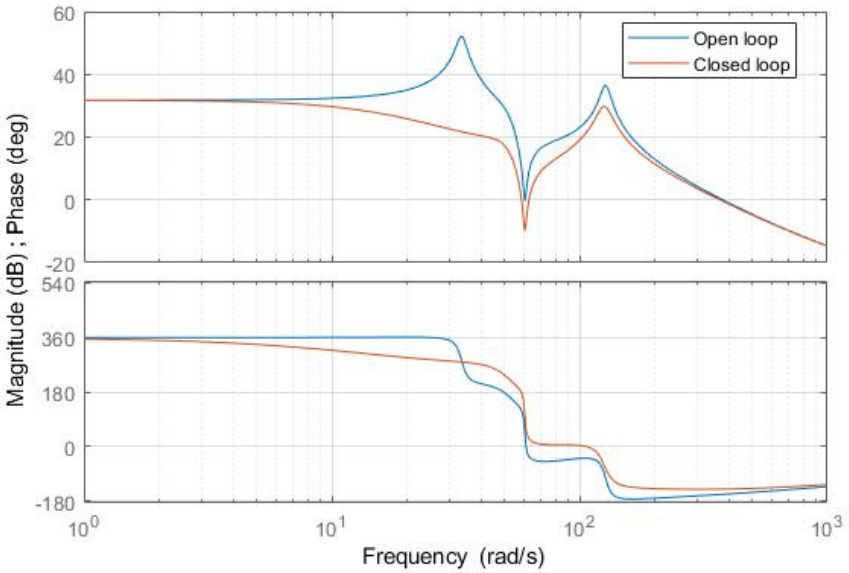

(a) Leading edge

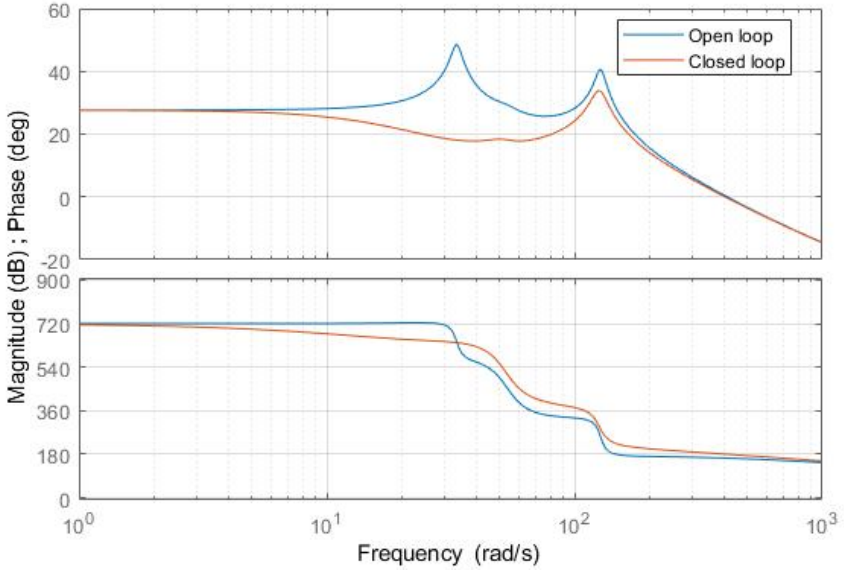

(b) Hinge line

Figure 5.5: Frequency response. Perfect, 80% flutter speed.

5.2 Case 2 : Perfect Actuator - 120% *Flutter*

A list of system poles and zeros is available in Appendix A.

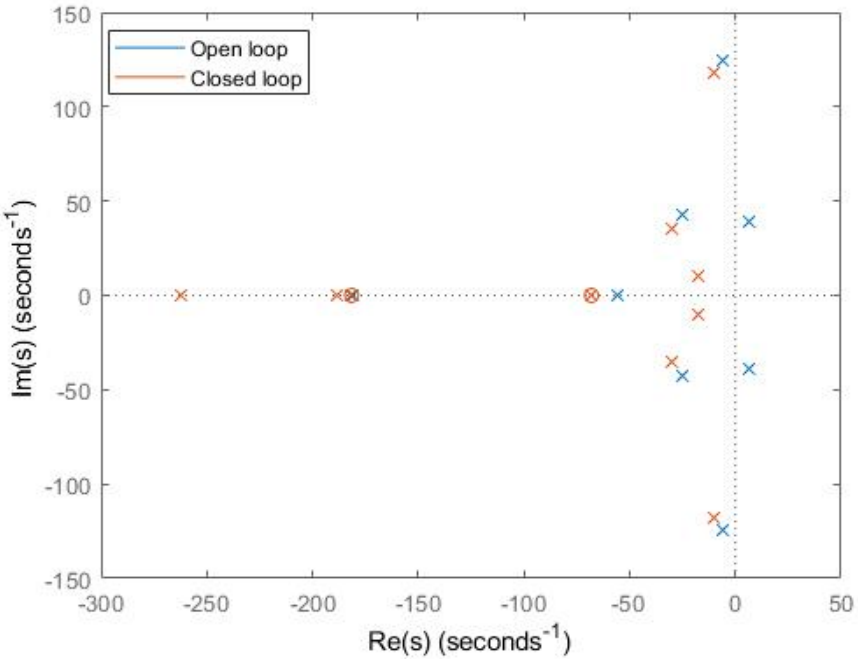

Figure 5.6: System poles and zeros. Perfect, 120% flutter speed.

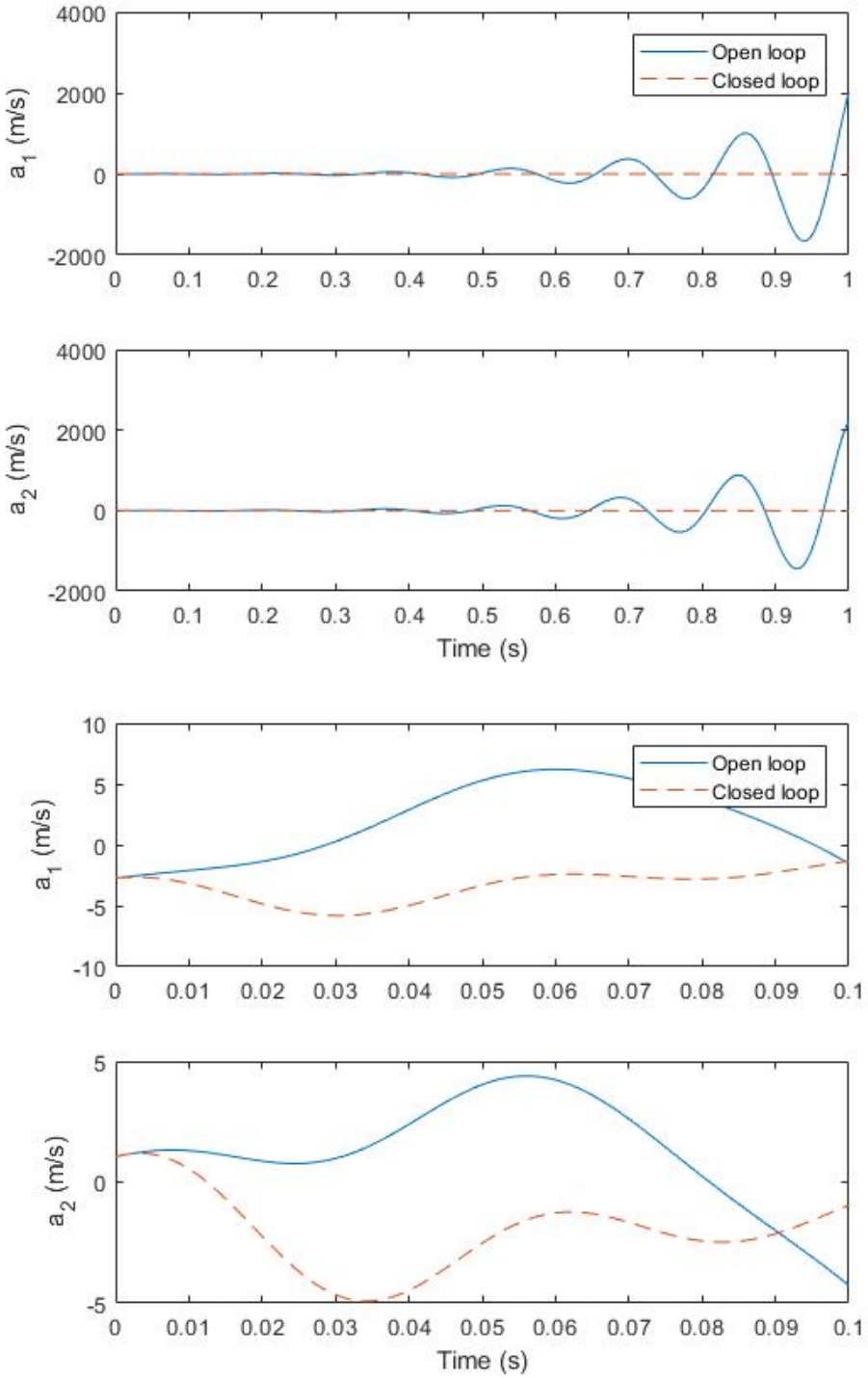

Figure 5.7: Time response to 2 degree perturbation in α. Perfect, 120% flutter speed.

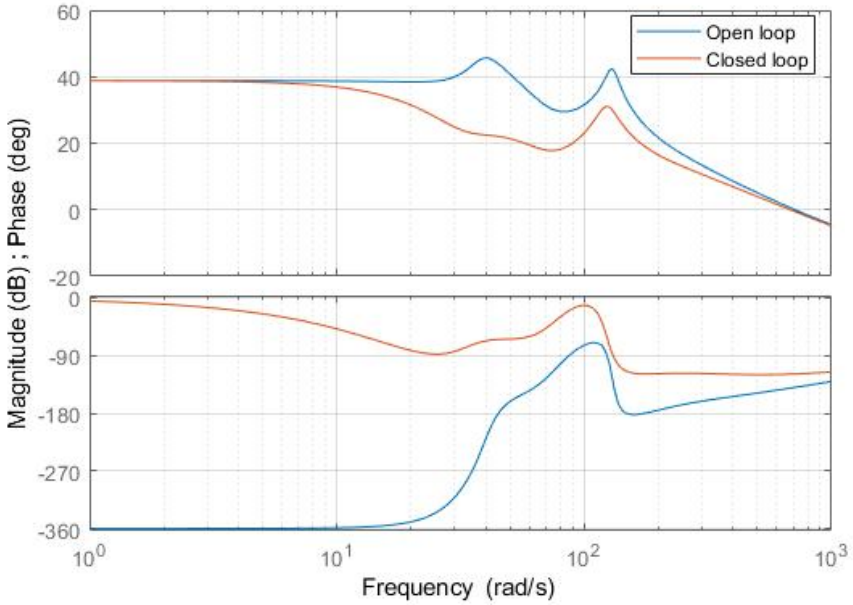

(a) Leading edge

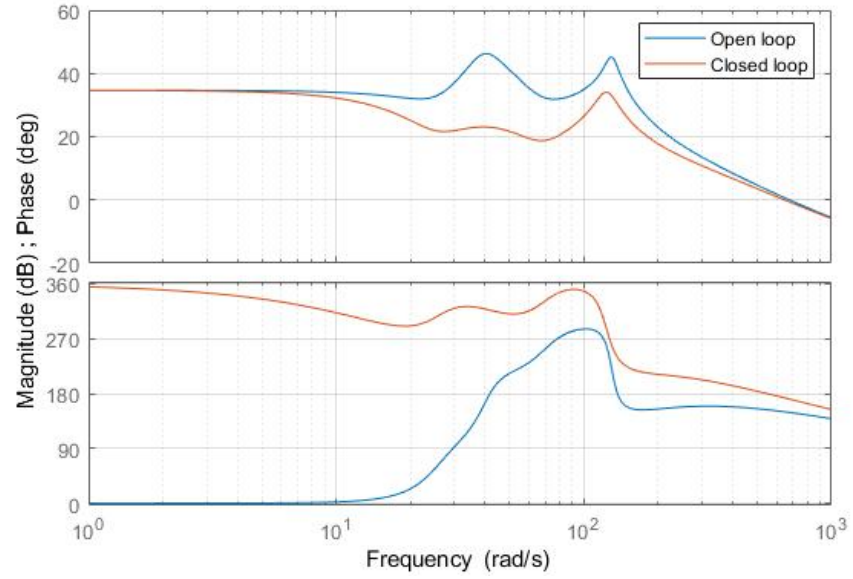

(b) Hinge line

Figure 5.8: Frequency response. Perfect, 120% flutter speed.

5.3 Case 3 : LOA - 80% *Flutter*

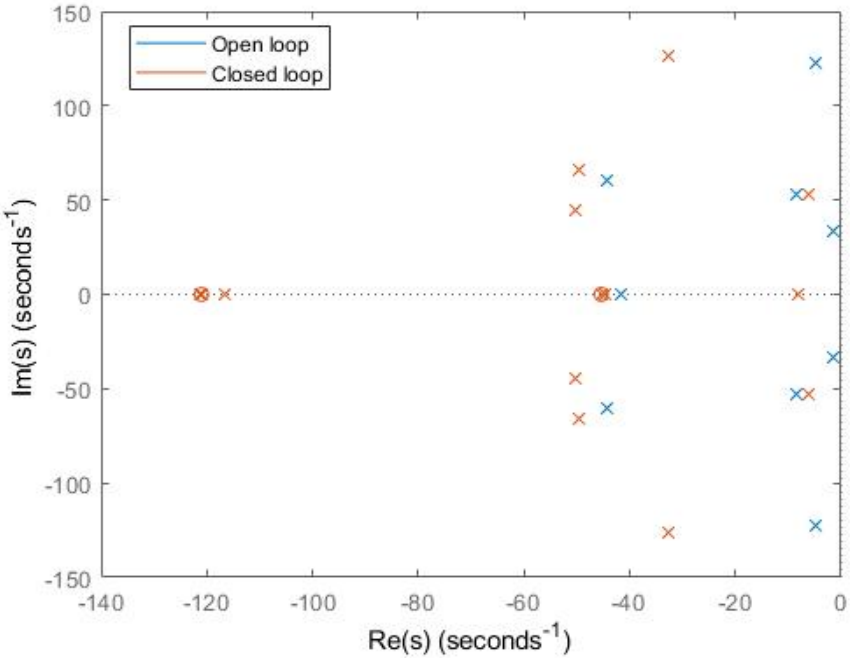

Figure 5.9: System poles and zeros. LOA, 80% flutter speed.

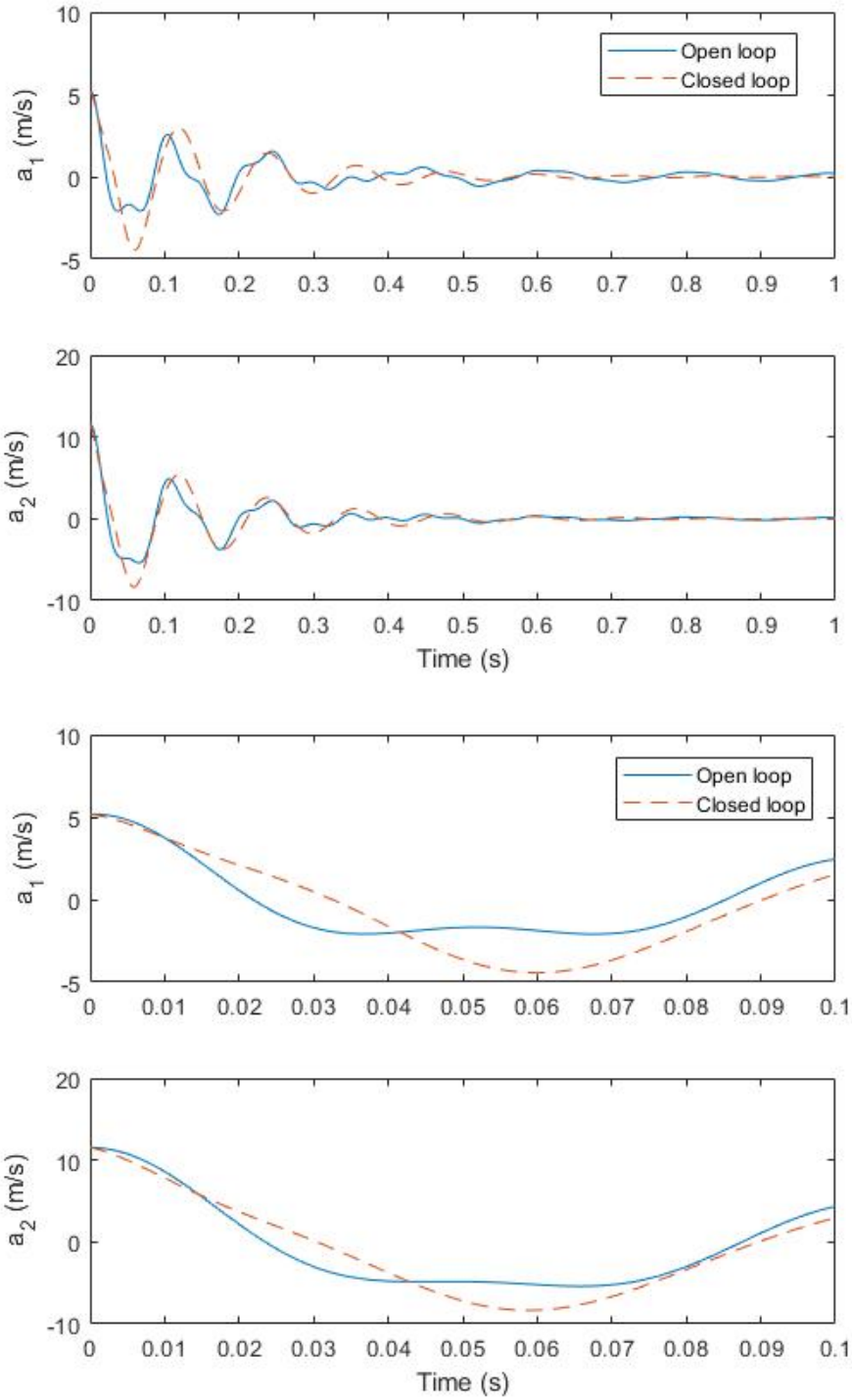

Figure 5.10: Time response to 2 degree perturbation in α. LOA, 80% flutter speed.

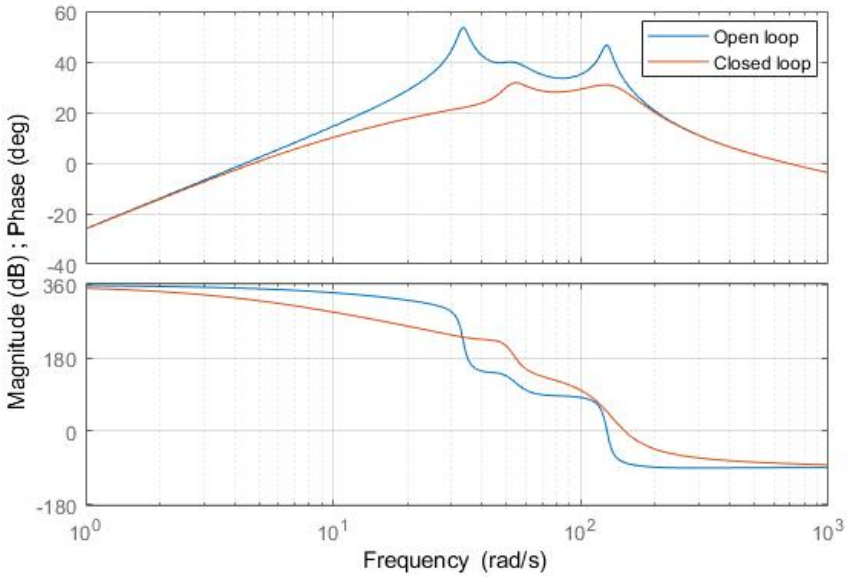

(a) Leading edge

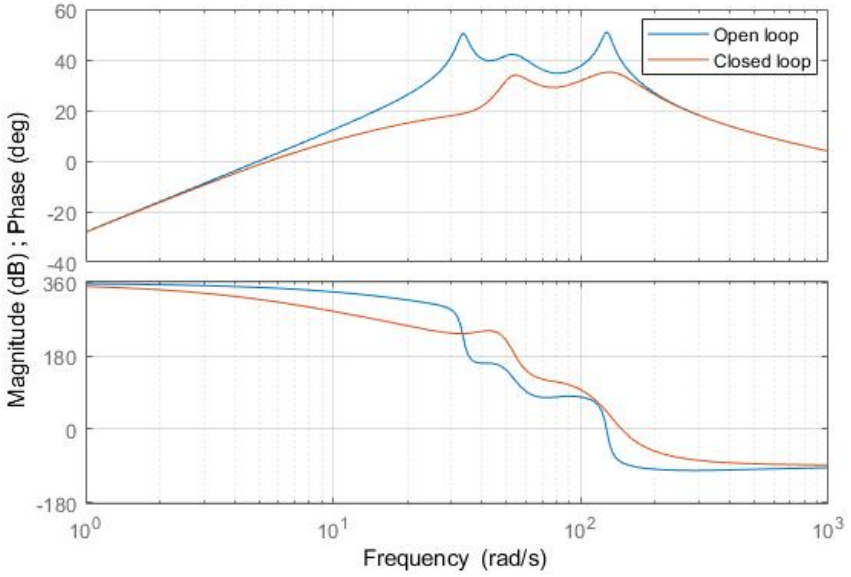

(b) Hinge line

Figure 5.11: Frequency response. LOA, 80% flutter speed.

5.4 Case 4 : LOA - 120% Flutter

A list of system poles and zeros is available in Appendix A.

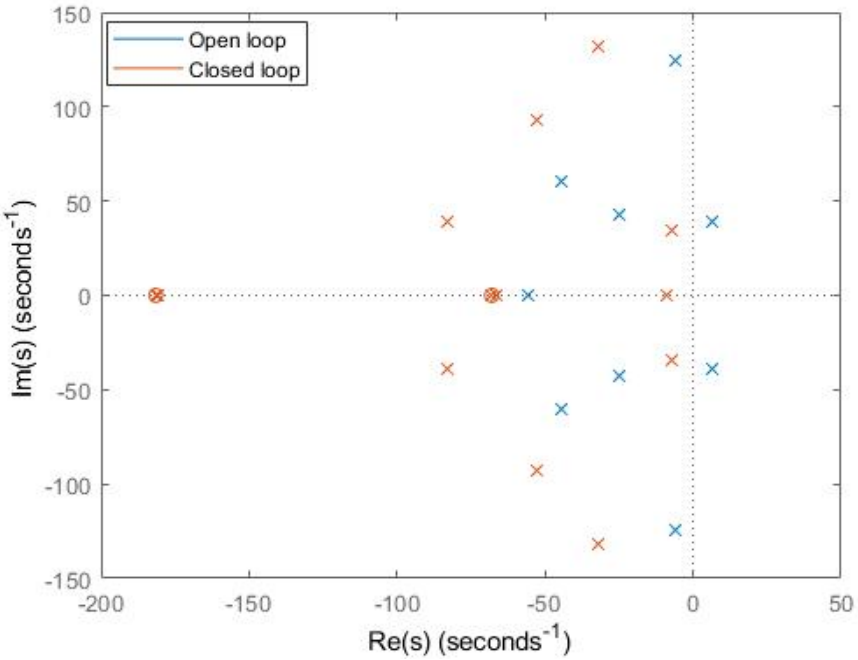

Figure 5.12: System poles and zeros. LOA, 120% flutter speed.

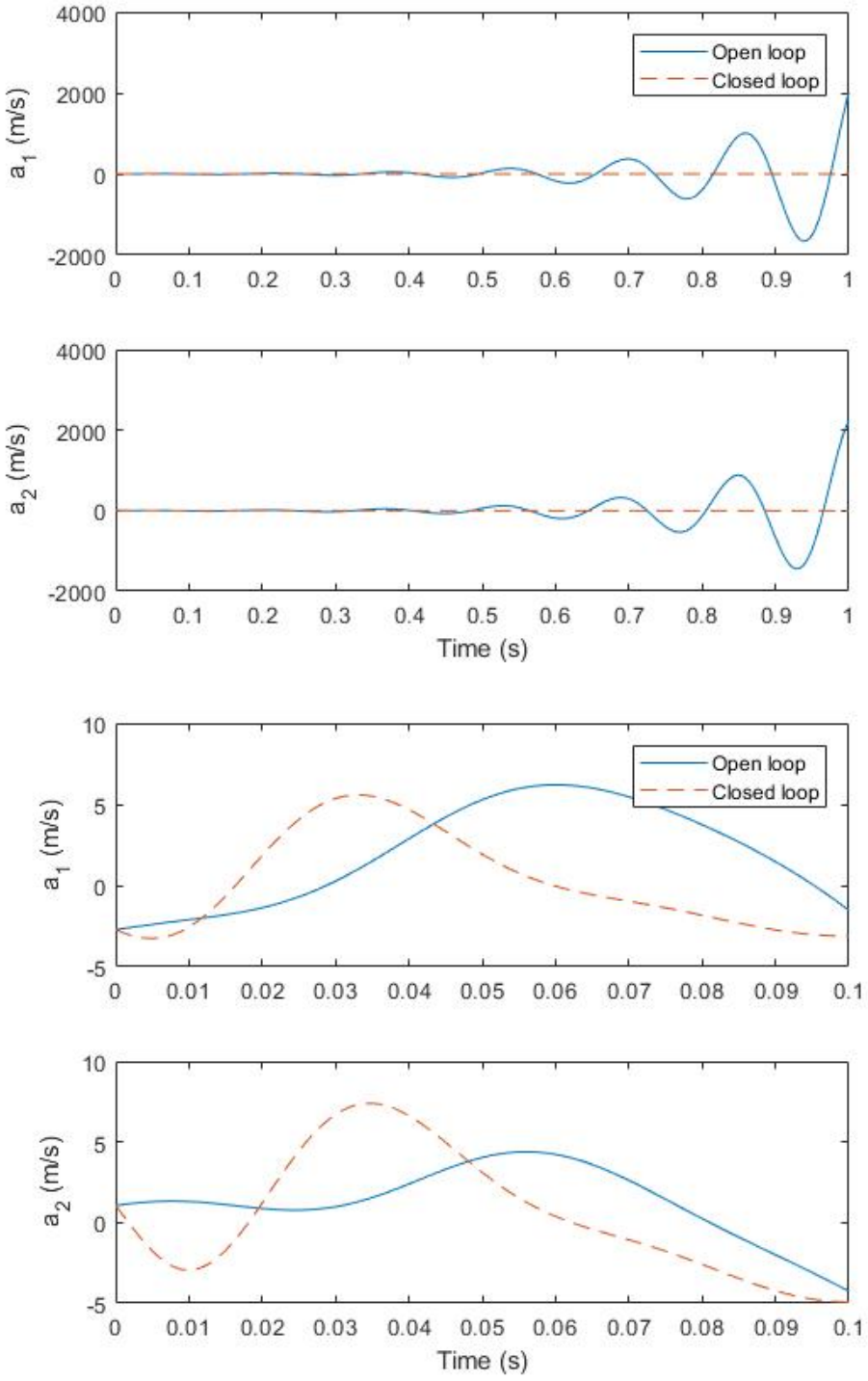

Figure 5.13: Time response to 2 degree perturbation in α. LOA, 120% flutter speed.

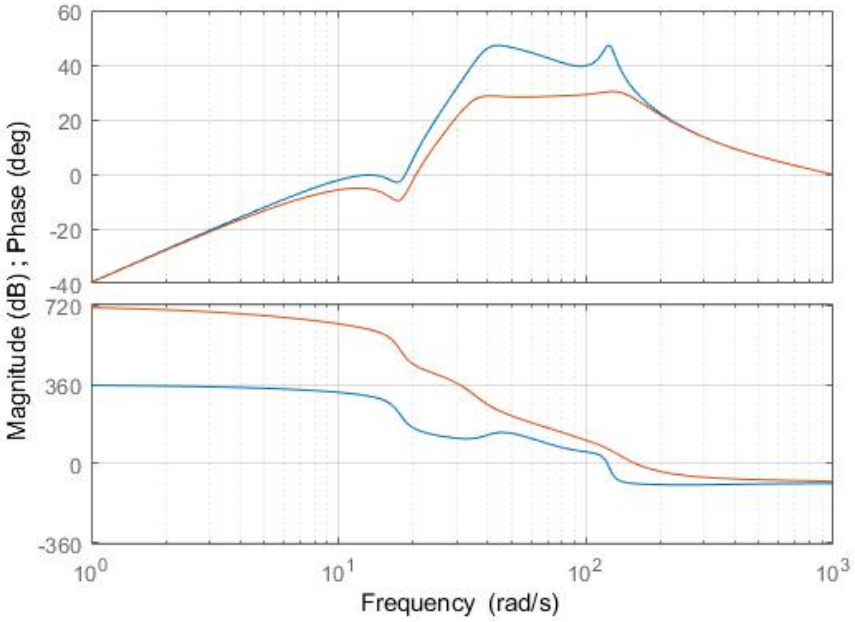

(a) Leading edge

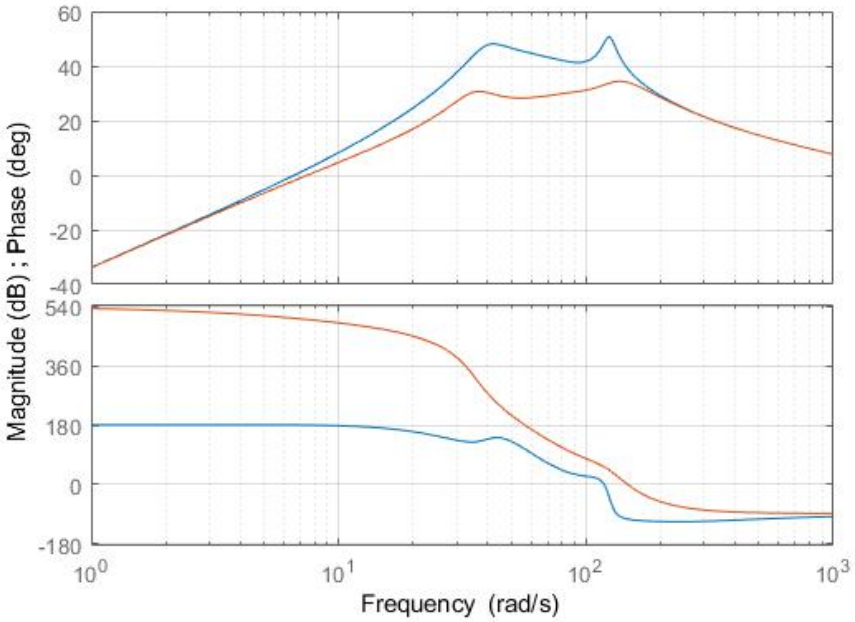

(b) Hinge line

Figure 5.14: Frequency response. LOA, 120% flutter speed.

5.5 Case 5 : HOA - 80% Flutter

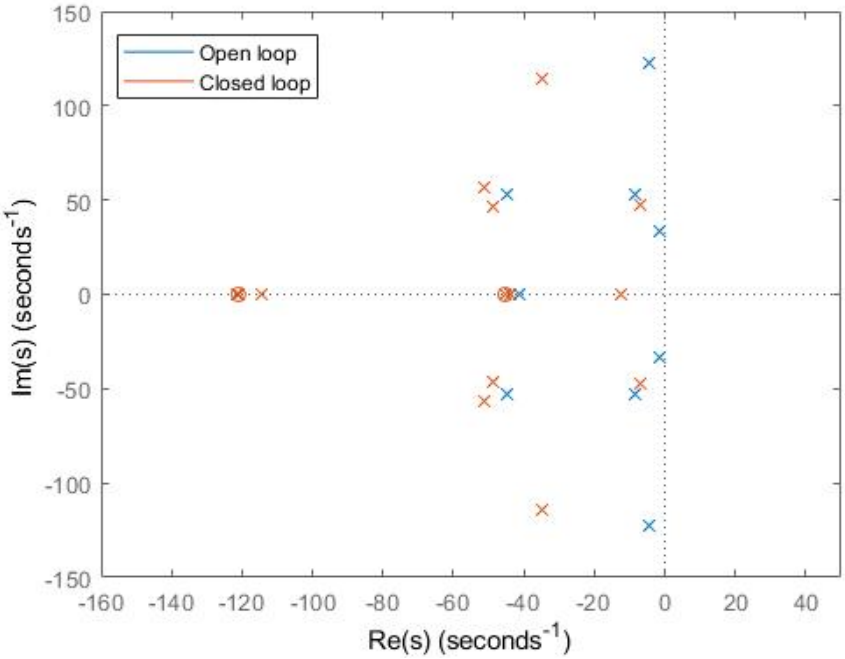

Figure 5.15: System poles and zeros. HOA, 80% flutter speed.

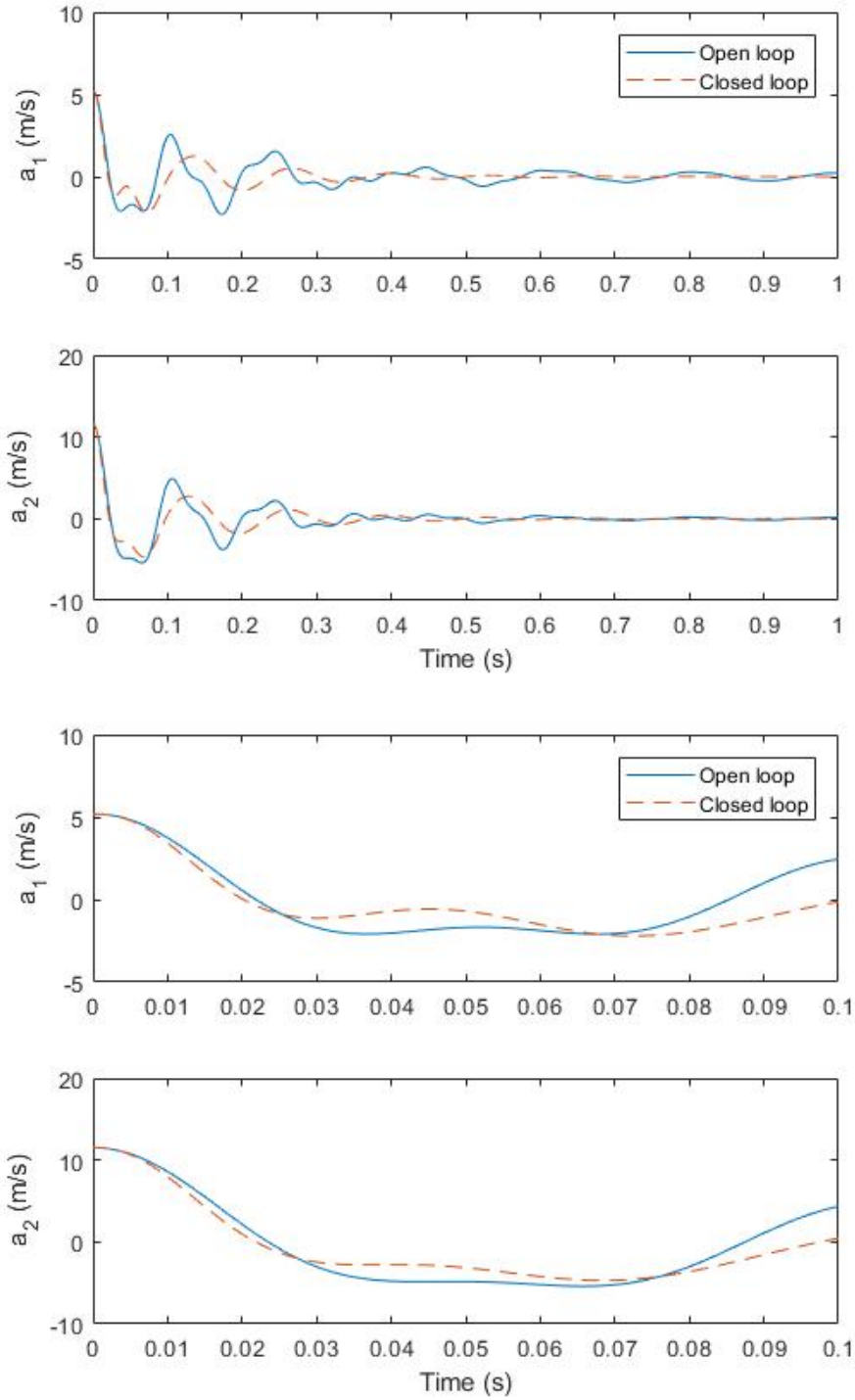

Figure 5.16: Time response to 2 degree perturbation in α. HOA, 80% flutter speed.

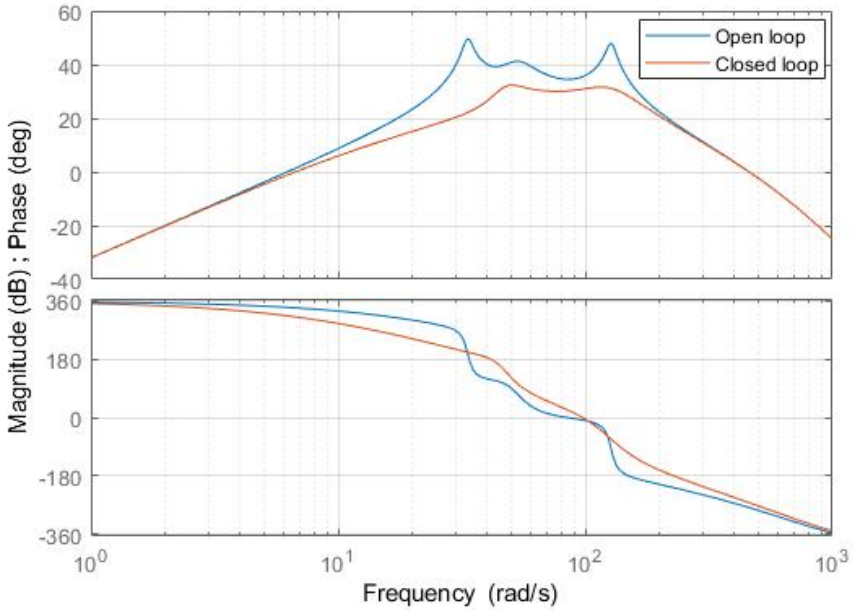

(a) Leading edge

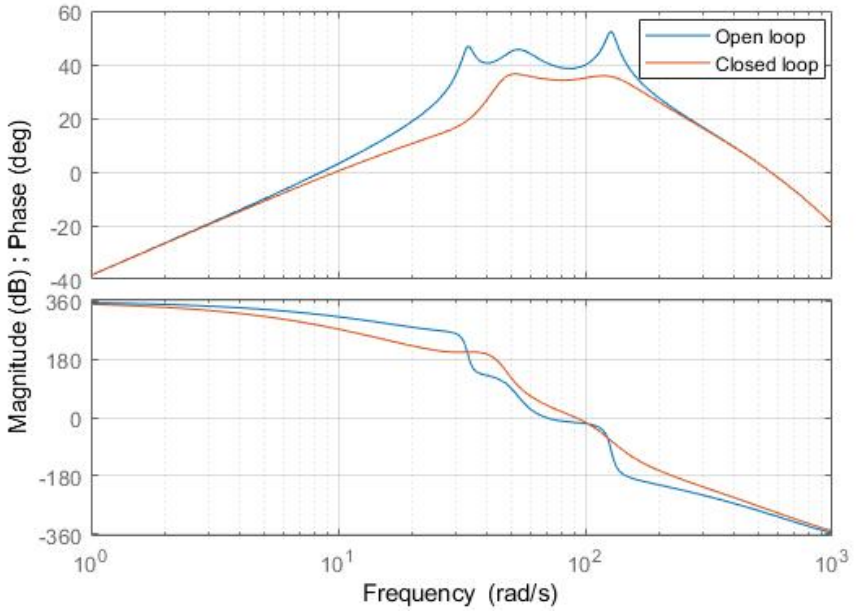

(b) Hinge line

Figure 5.17: Frequency response. HOA, 80% flutter speed.

5.6 Case 6 : HOA - 120% *Flutter*

A list of system poles and zeros is available in Appendix A.

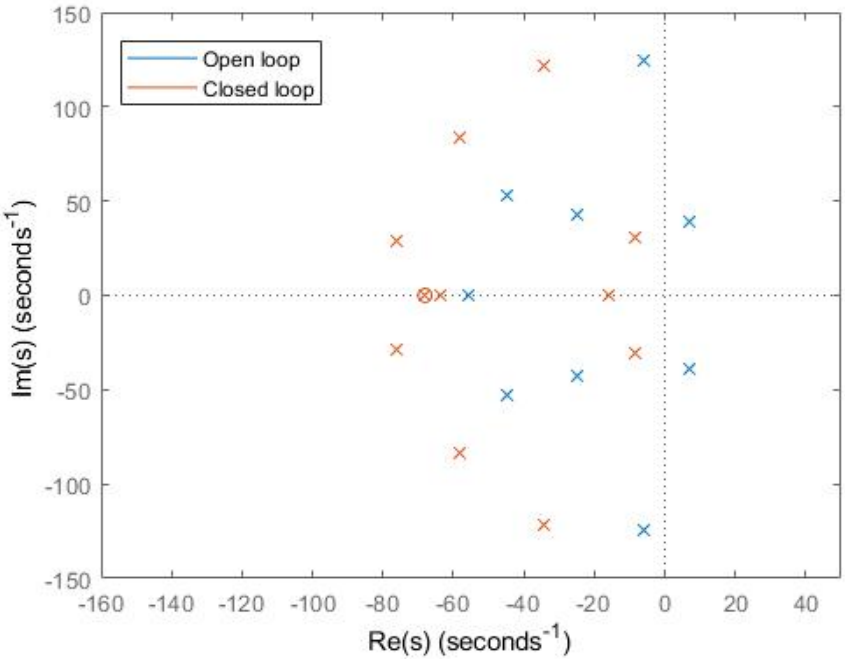

Figure 5.18: System poles and zeros. HOA, 120% flutter speed.

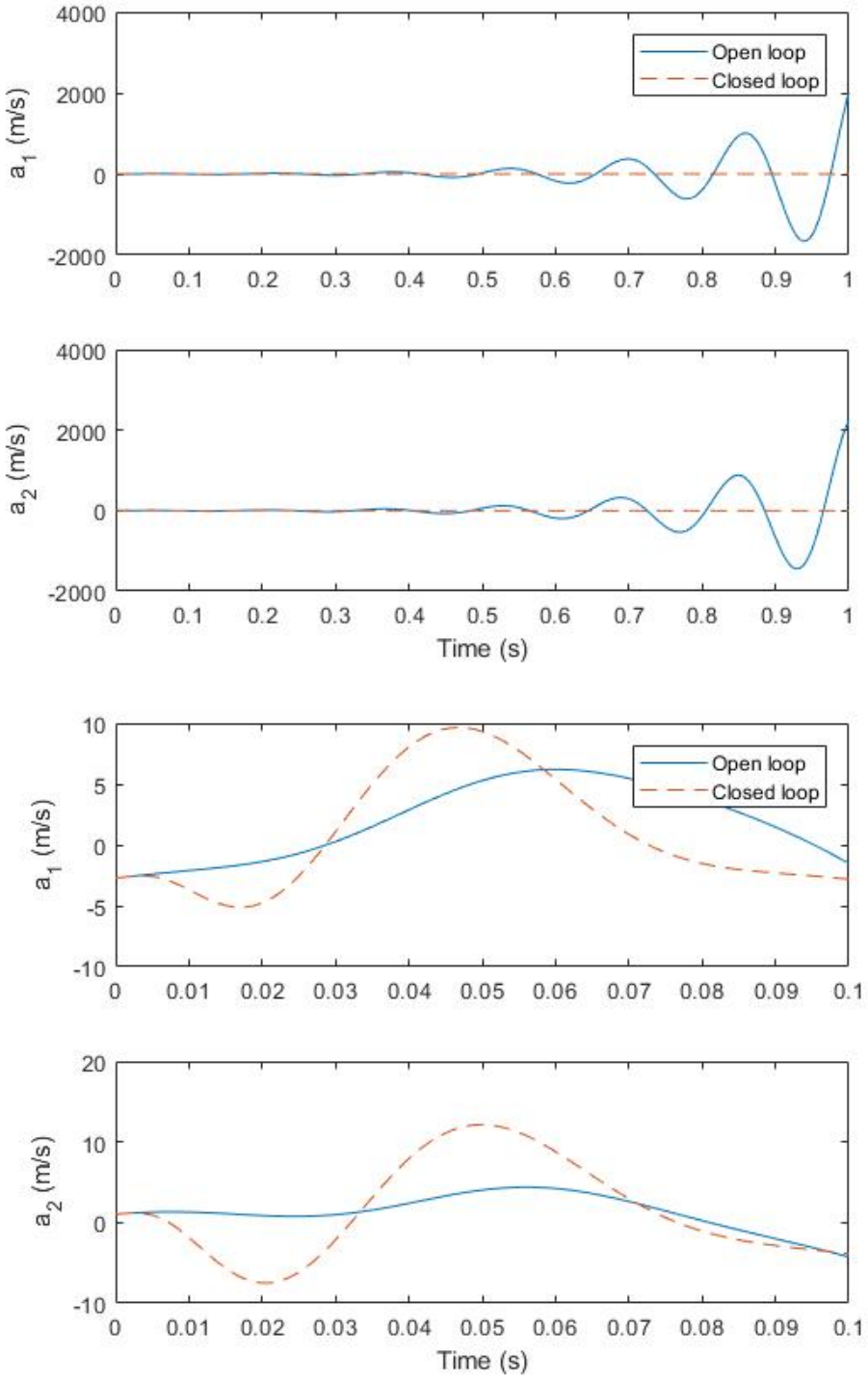

Figure 5.19: Time response to 2 degree perturbation in α. HOA, 120% flutter speed.

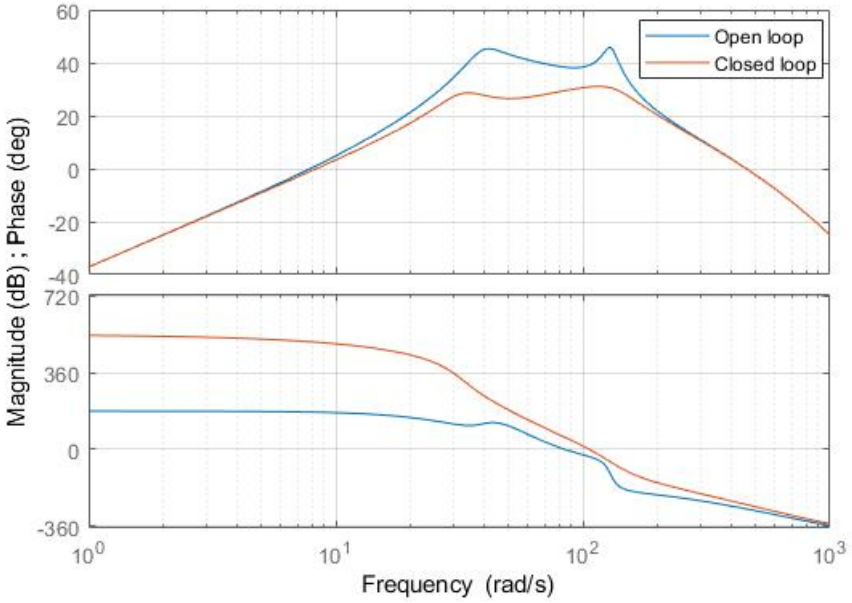

(a) Leading edge

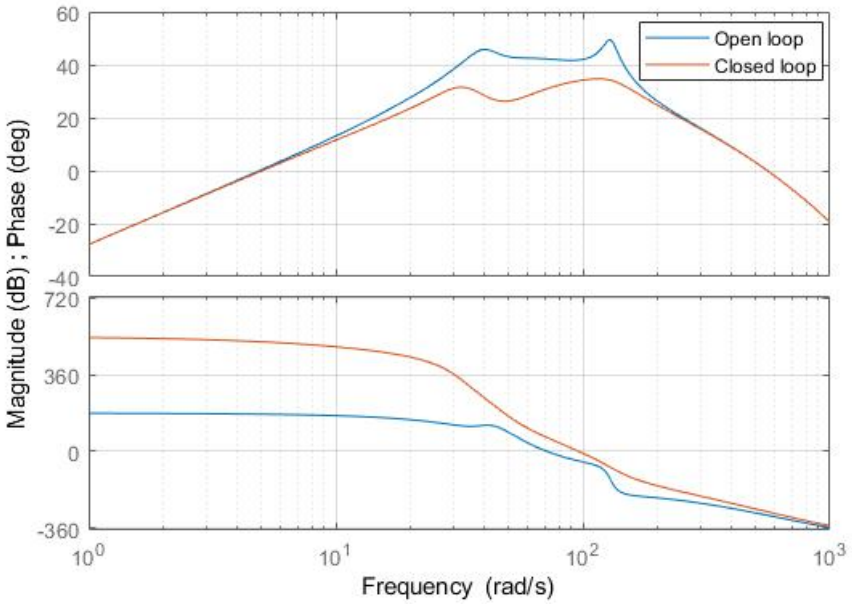

(b) Hinge line

Figure 5.20: Frequency response. HOA, 120% flutter speed.

5.7 Case 7 : HOA - 120% Flutter - $2 \times k_{max}$

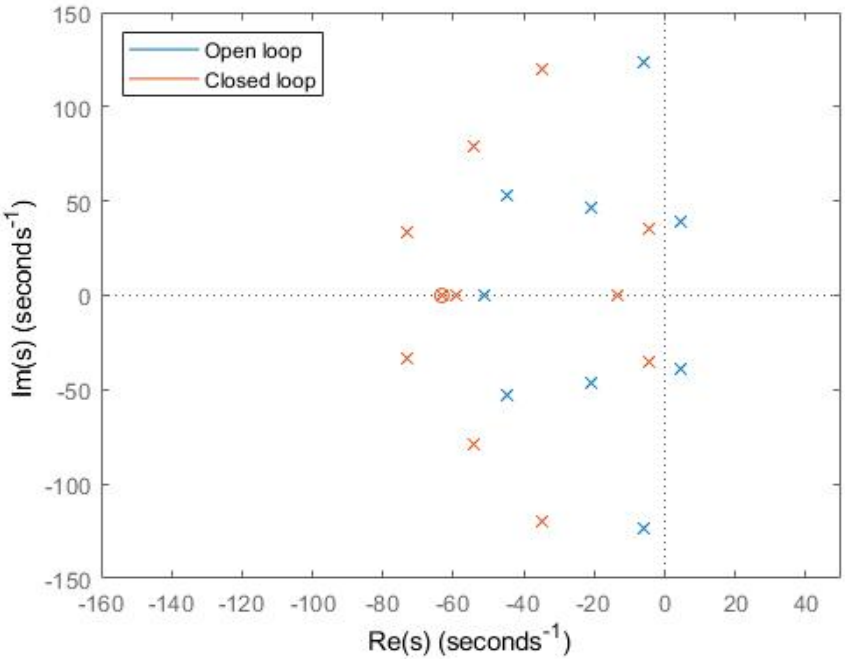

Figure 5.21: System poles and zeros. HOA, 120% flutter speed, $2 \times k_{max}$

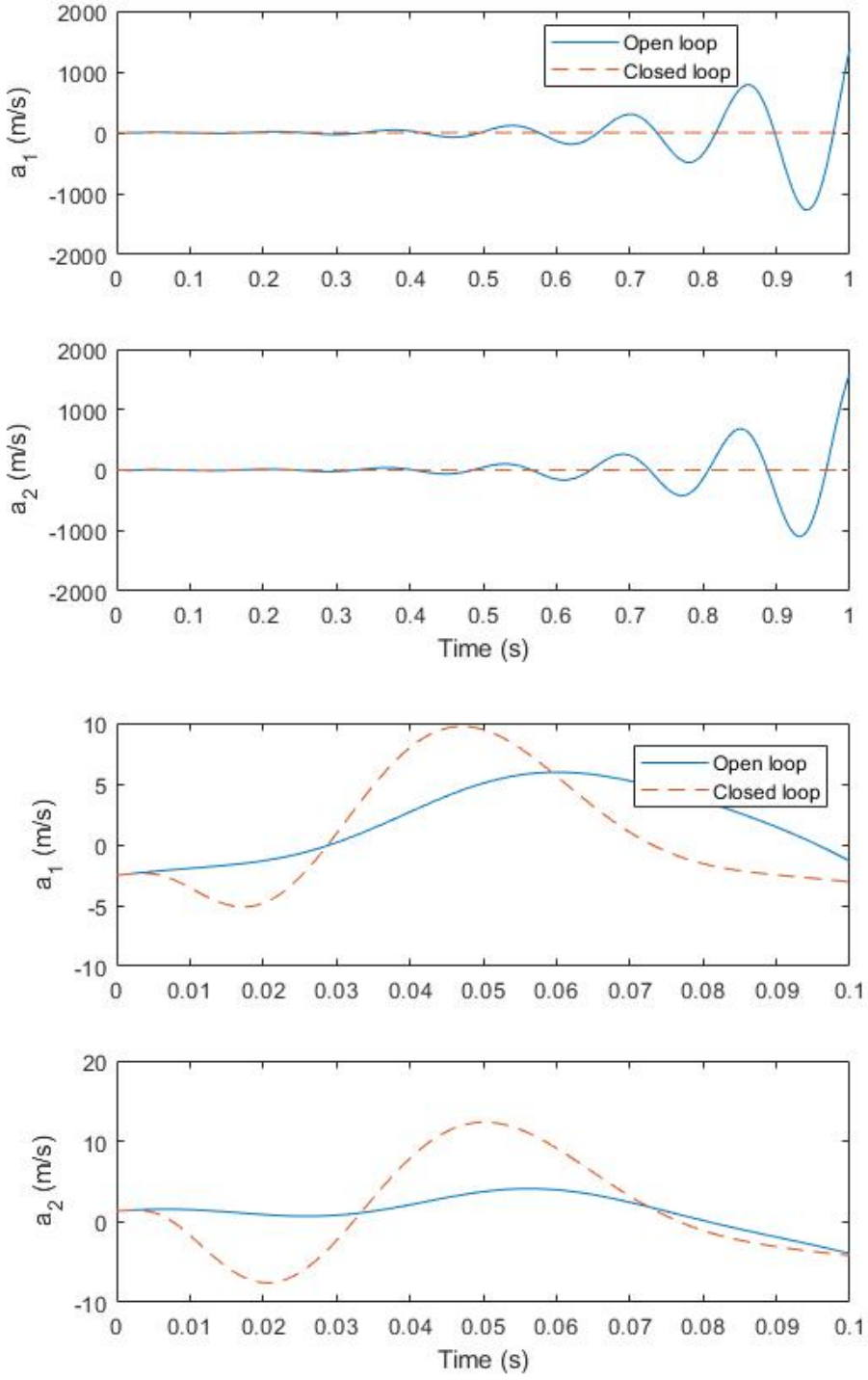

Figure 5.22: Time response to 2 degree perturbation in α. HOA, 120% flutter speed, $2 \times k_{max}$

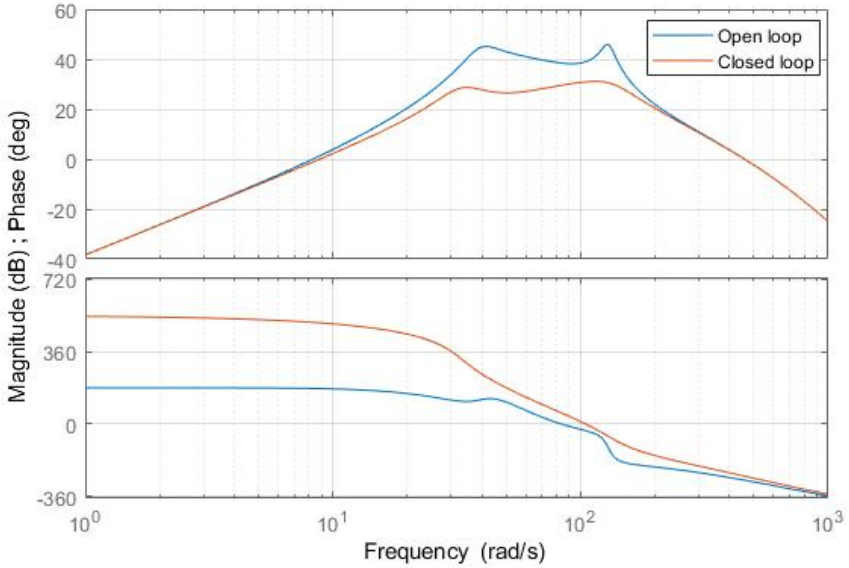

(a) Leading edge

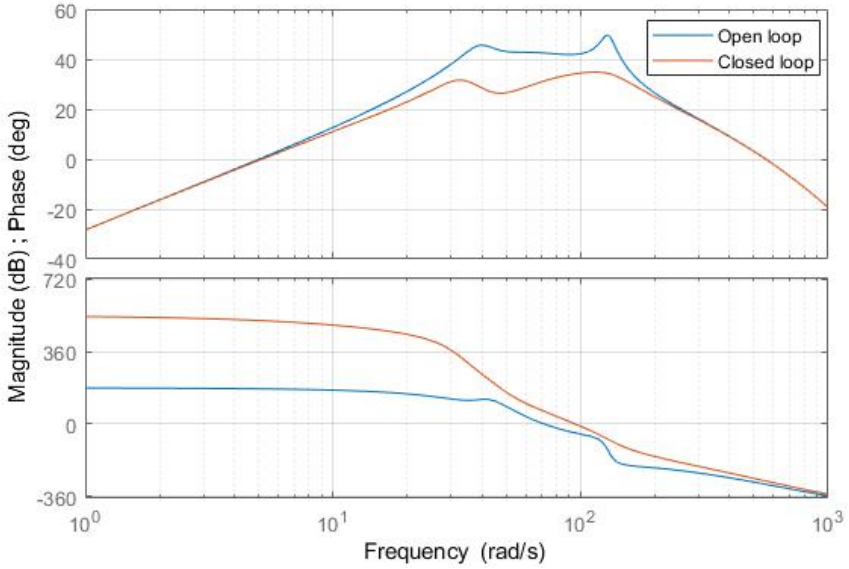

(b) Hinge line

Figure 5.23: Frequency response. HOA, 120% flutter speed, $2 \times k_{max}$

Chapter 6

DISCUSSION

After comparing all of the cases completed at 80% flutter speed or 120% flutter speed, it was determined that there were no significant differences, with the exception of the Case 1 and Case 4 frequency response measured at the leading edge (Figures 5.5.a and 5.11.a). Case 1, which does not include actuator dynamics, showed a "dip" in both the closed loop and open loop response at 60.17 rad/s. Case 4, which includes low order actuator dynamics, showed a "dip" in both the closed loop and open loop response at 17.08 rad/s. For both cases, the response measured at the hinge line did not show a similar "dip", and the "dip" could be flattened by increasing or decreasing the speed, with full removal of the "dip" occurring around $\pm 15\% U_{flutter}$ from the original speed. To investigate this further, the controllability and observability for each case was determined using the following method.

6.1 Controllability and Observability

Controllability was determined by starting with

$$\dot{x} = Ax + Bu \tag{6.1}$$

The eigenvectors of A were found and placed column by column in matrix Φ. Then, x was transformed using

$$x = \Phi\eta \tag{6.2}$$

Taking another step:

$$\dot{\eta} = \Phi^{-1}A\Phi\eta + \Phi^{-1}Bu \tag{6.3}$$

But

$$\Phi^{-1} A \Phi = [\lambda] \tag{6.4}$$

So now the equations are coupled. On the right hand side:

$$\tilde{B} = \Phi^{-1} B \tag{6.5}$$

If any row of $\tilde{B}$ is zero, the corresponding state is uncontrollable.

Likewise, to determine observability, C was transformed to $\tilde{C}$ by

$$\tilde{C} = C\Phi \tag{6.6}$$

If any column of $\tilde{C}$ is zero, the corresponding state is unobservable.

The transformed B and C matrices for Cases 2, 4, and 6 are shown in Appendix B.

6.2 Lessons Learned

Through this controllability and observability test, it was determined that all the states were controllable for all cases. For observability, five aerodynamic lag states were always unobservable. But more interestingly, for Case 4, the second structural mode, α, becomes unobservable, then observable as the "dip" in the frequency response flattened for the leading edge sensor. Once below flutter speed, the first structural mode, h, became unobservable, before switching to unobservable for the third structural mode β, then returning to all structural modes being observable. Likewise, for Case 1 with no actuator dynamics, the second structural state becomes less observable near conditions of the "dip". It was also discovered that moving the leading edge sensor aft increased observability and eventually removed the "dip" in the frequency response. Therefore, it was determined that the discrepancy between leading edge frequency responses could be due to sensor placement and/or interaction with actuator dynamics. Thus, for the purposes of this study, only hinge line

frequency responses were considered. Since no significant differences in time or frequency responses were observed at the hinge line sensor, it is concluded that neither actuator order nor Roger approximation frequency range significantly affects LQR performance. It is also concluded that optimal sensor placement should be verified with each set of actuators used.

Chapter 7
CONCLUSION

From this investigation, several conclusions can be made. For this simple system, actuator order has little effect on system response. Also, Roger approximation upper frequency validity bound does not affect the cases studied here. Lack of system dynamics at high frequencies and filtering effects of actuators makes it insensitive to aerodynamic model high frequencies, and LQR assumes state space model is valid at all frequencies. Observability must be reverified as new actuators are implemented into a system. Bottom line, the need of developing an aeroservoelastic simulation capability was successfully achieved.

7.1 Recommendations

Several additions can be improve the functionality of the simulation capability. Other rational function approximations could be added to the code and compared to Roger approximation results. An algorithm which optimizes aerodynamic lag terms could be included. Other controllers could be developed and tested. An estimator could be added, as well as sensor dynamics.

BIBLIOGRAPHY

[1] E. Livne, "Aircraft active flutter suppression: State of the art and technology maturation needs," *Journal of Aircraft*, vol. 55, pp. 410–452, 2018.

[2] J. I. Arnold and J. B. Dempster, "Flight test evaluation of an advanced stability augmentation system for b-52 aircraft," *Journal of Aircraft*, vol. 6, no. 4, pp. 343–348, 1969.

[3] E. Livne, "Future of airplane aeroelasticity," *Journal of Aircraft*, vol. 40, no. 6, pp. 1066–1092, 2003.

[4] M. R. Waszak and D. K. Schmidt, "Flight dynamics of aeroelastic vehicles," *Journal of Aircraft*, vol. 25, no. 6, pp. 563–571, 1988.

[5] *ZAERO Users Manual*, 9th ed., ZONA Technology, Inc., Scottsdale, AZ, 1 2016.

[6] Composite Design Solutions, "Design and engineering services," 2018, [Online; accessed February 22, 2018]. [Online]. Available: http://www.compositedesignsolutions.com/

[7] K. L. Roger, G. E. Hodges, and L. Felt, "Active flutter suppression − a flight test demonstration," *Journal of Aircraft*, vol. 12, no. 6, pp. 551–556, 1988.

[8] E. Livne, "AA 554 HW6."

[9] M. Karpel, "Design for active flutter suppression and gust alleviation using state space aeroelastic modeling," *Journal of Aircraft*, vol. 19, no. 3, pp. 221–227, 1982.

[10] E. Livne, "ASE Equations in State Space."

[11] M. D. Conner, D. M. Tang, E. H. Dowell, and L. N. Virgin, "Nonlinear behavior of a typical airfoil section with control surface freeplay: A numerical and experimental study," *Journal of Fluids and Structures*, vol. 11, no. 1, pp. 89–109, 1997.

[12] M. Brenner, "Aeroservoelastic modeling and validation of a thrust vectoring F/A-18 aircraft," NASA, Tech. Rep. 4494, June 1993.

Appendix A

POLES AND ZEROS

Open Loop	Closed Loop
6.7500±39.3227i	-9.9294±117.8836i
-6.1954±124.1352i	-17.72±9.9709i
-25.1401±42.8975i	-30.3147±35.1567i
-55.9200	-262.5207
-68.0627	-68.0627
-68.0627	-68.0627
-68.0627	-68.0627
-181.5005	-181.5031
-181.5005	-181.5032
-181.5005	-181.5032
-181.2124	-188.5261

Table A.1: Poles of open and closed loop system. Perfect, 120% flutter speed.

-68.0600
-68.0600
-181.5000
-181.5000

Table A.2: Zeros of the system. Perfect, 120% flutter speed.

Open Loop	Closed Loop
6.7500± 9.3227i	-7.0911±34.7649i
-25.1401±42.8975i	-82.9352±38.5702i
-44.25-60.5552i	-52.5314-93.2717i
-44.25+60.5552i	-52.5314+93.2717i
-6.1954-124.1352i	-32.1530-131.4314i
-6.1954+124.1352i	-32.1530+131.4314i
-55.9200	-8.9582
-68.0627	-66.6047
-68.0627	-68.0627
-68.0627	-68.0627
-181.2124	-180.7528-0.3090i
-181.5004	-180.7528+0.3090i
-181.5004	-181.5005-5.2705E-13i
-181.5004	-181.5005+5.2705E-13i

Table A.3: Poles of open and closed loop system. LOA, 120% flutter speed.

-68.0630
-68.0630
-68.0630
-181.5000
-181.5000
-181.5000

Table A.4: Zeros of the system. LOA, 120% flutter speed.

Open Loop	Closed Loop
6.75001±39.3227i	-8.50076±30.7585i
-6.195376±124.1352i	-34.5242±122.0485i
-25.1401±42.8975i	-58.2065±83.8201i
-44.915±52.5115i	-68.0627
-55.92	-15.6968
-68.0627	-63.6730
-68.0627±1.0950e-14i	-76.2988±29.0539i
-181.2124	-179.3581
-181.5004	-181.1947
-181.5004	-181.5004
-181.5004	-181.5004
-368.48±133.7404i	-364.2213±137.9089i
-611.72±426.9832i	-611.6908±426.0152i
-17326	-17326

Table A.5: Poles of open and closed loop system. HOA, 120% flutter speed.

-68.0630
-68.0630
-181.5000
-181.5000

Table A.6: Zeros of the system. HOA, 120% flutter speed.

Appendix B

CONTROLLABILITY AND OBSERVABILITY

-27.9564-3.84051i	-0.1172-0.15391i	-0.010523-0.00072996i
-27.9564+3.84051i	-0.1172+0.15391i	-0.010523+0.00072996i
75.19-5.0022e-14i	3.784-1.3399E-15i	0.012107-3.9254E-18i
-82.6975-35.4878i	0.10838-1.4024i	0.0020121-0.0031949i
-82.6975+35.4878i	0.10838+1.4024i	0.0020121+0.0031949i
-11.004+36.264i	1.4292+1.1576i	0.0074704+0.003257i
-11.004-36.264i	1.4292-1.1576i	0.0074704-0.003257i
-26.3358+1.42676E-15i	-1.6418+1.8902E-16i	-0.0060738+5.7146E-19i
7.6559-2.562E-15i	0.21054-7.003E-17i	0.00060942-2.2088E-19i
0.098388+9.4361E-16i	-0.10667+2.1089E-17i	-0.0002841+6.0685E-20i
-29.2983+1.62459E-15i	-2.0313+2.4447E-16i	-0.007881+7.3176E-19i
5.433-3.4487E-16i	0.47589-6.8378E-17i	0.002167-1.9879E-19i
0	1	0
0	1	0

Table B.1: Transformed B Matrix. Perfect, 120% flutter speed.

22.4083+22.9292i	22.4083-22.9292i	43.1427	-4.10118+15.8898i	-4.10118-15.8898i	8.0003+29.3397i	8.0003-29.3397i	44.1328	-2.2476E-11	5.6063E-12	-2.9616E-10	-7.8040E-11
41.1106+22.0003i	41.1106-22.0003i	53.4092	-9.1206+12.4651i	-9.1206-12.4651i	21.0169+35.0988i	21.0169-35.0988i	58.6041	-2.5493E-11	5.3922E-12	-3.9702E-10	-1.0563E-10
Continued											
2.8422E-13	5.4001E-13										
2.2737E-13	9.8055E-13										

Table B.2: Transformed C Matrix. Perfect, 120% flutter speed.

-52.4325-6.4332E-13i
-7.1880-1.7685E-13i
16.2764-40.0159i
16.2764+40.0159i
51.1355-10.3667i
51.1355+10.3667i
-144.8931+183.5046i
-144.8931-183.5046i
214.8456-9.3394E-14i
-32.4108-4.4540E-13i
7.6600-1.7431E-15i
-2.2777+1.3404E-15i
-90.1956-1.3861E-14i
-46.5850-3.6482E-15i
93.7830-194.5769i
93.7830+194.5769i

Table B.3: Transformed B Matrix. LOA, 120% flutter speed.

-44.1328	-5.7518E-11	22.4083+22.9292i	22.4083-22.9292i	4.10118-15.8898i	4.1012+15.8898i	8.0003+29.3397i	8.0003-29.3397i	-43.1427	5.2744E-11	1.9701E-11	-7.6629E-12
-58.6041	-7.2718E-11	41.1106+22.0003i	41.1106-22.0003i	9.1206-12.4651i	9.1206+12.4651i	21.0169+35.0988i	21.0169-35.0988i	-53.4092	7.4286E-11	2.1469E-11	-9.4413E-12
0	0	0	0	0	0	0	0	0	0	0	0
0	0	0	0	0	0	0	0	0	0	0	0
0	0	0	0	0	0	0	0	0	0	0	0
Continued											
-2.1007E-13	6.6791E-13	17.2486+38.8284i	17.2486-38.8284i								
-1.9506E-13	2.0037E-12	41.4237+46.6662i	17.2486-38.8284i								
0	0	0.1937-0.0934i	0.1937-0.0933i								
0	0	-2.9178+15.8608i	-2.9178-15.8608i								
0	0	-834.0647-862.7574i	-834.0647+862.7574i								

Table B.4: Transformed C Matrix. LOA, 120% flutter speed.

-48.3245-12.0189i
-48.3245+12.0189i
209.5526+2.1388E-12i
-36.9914+3.0868i
-36.9914-3.0868i
-4.0202+273.6069i
-4.0202-273.6069i
-35.2132-4.0852E-13i
5.1275+5.4430E-14i
39.1910+4.4925E-13i
4.0366+4.0535E-14i
-66.8593+95.0960i
-66.8593-95.0960i
-88.9342-9.2798E-13i
46.6915+301.4943i
46.6915-301.4943i
79.8677+5.0878i
79.8677-5.0878i
140.8027+23.0186i
140.8027-23.0186i
1.4520

Table B.5: Transformed B Matrix. HOA, 120% flutter speed.

22.4083+22.9292i	22.4083-22.9292i	-43.1426	-4.1011+15.8898i	-4.1011-15.8898i	8.0003+29.3397i	8.0003-29.3397i	-44.1328	7.5910E-13	-5.0763E-10	1.4084E-11	-1.5703e-13-6.6955e-14i
41.1106+22.0003i	41.1106-22.0003i	-53.4091	-9.1206+12.4651i	-9.1206-12.4651i	21.0169+35.0988i	21.0169-35.0988i	-58.6041	-1.1976E-12	-6.7356E-10	1.6944E-11	-2.7605e-13-7.73e-14i
0	0	0	0	0	0	0	0	0	0	0	0
0	0	0	0	0	0	0	0	0	0	0	0
0	0	0	0	0	0	0	0	0	0	0	0
Continued											
-1.5703E-13+6.6955E-14i	-1.3074E-12	-10.7552-40.7544i	-10.7552+40.7544i	-3.8139-2.5062i	-3.8139+2.5062i	7.5701+2.2356i	7.5701-2.2356i	-6.2544E-4			
-2.7605E-13+7.73E-14i	-1.62E-12	-31.0196-52.2115i	-31.0196+52.2115i	-7.2108-4.8097i	-7.2108+4.8097i	14.5233+4.8369i	14.5233-4.83693i	1.191E-3			
0	0	-0.1808+0.0139i	-0.1808-0.0139i	-0.0597-0.0439i	-0.0597+0.0439i	0.1313+0.0568i	0.1313-0.0568i	-9.7365E-6			
0	0	7.3928-10.1231i	7.3928+10.1231i	55.3143+1.3992i	55.3143-1.3992i	-56.0045-3.3668i	-56.0045+3.3668i	0.1686			
0	0	199.5297+842.8922i	199.5297-842.8922i	34434.3133-22762.2904i	34434.3133+22762.2904i	21086.8216-6249.4466i	21086.8216+6249.4466i	2922.7152			

Table B.6: Transformed C Matrix. HOA, 120% flutter speed.